RSC Advances

PAPER

View Article Online
View Journal | View Issue



Cite this: *RSC Adv.*, 2025, **15**, 12896

# Targeting VEGFR-2 in breast cancer: synthesis and *in silico* and *in vitro* characterization of quinoxaline-based inhibitors†

Ibrahim H. Eissa, *[a] Alaa Elwan, [a] Mustafa A. Al-Qadhi, [b] Dalal Z. Husein, [c] Fatma G. Amin, [d] Aisha A. Alsfouk, [e] Eslam B. Elkaeed, [f] Hazem Elkady *[a] and Ahmed M. Metwaly *[g]

A novel series of quinoxaline derivatives was designed and synthesized to target VEGFR-2, a receptor critical in cancer progression, with a focus on favorable pharmacophoric features. Among these derivatives, compound **11d** emerged as a promising candidate, exhibiting potent cytotoxicity against MDA-MB-231 and MCF-7 cancer cell lines, with $IC_{50}$ values of 21.68 μM and 35.81 μM, respectively, while displaying significantly reduced toxicity in normal cell lines WI-38 and WISH ($IC_{50}$ values of 82.46 μM and 75.27 μM). Compared to standard treatments doxorubicin and sorafenib, compound **11d** demonstrated a favorable therapeutic window. Inhibition assays showed that **11d** inhibits VEGFR-2 with an $IC_{50}$ of 62.26 nM ± 2.77, comparable to sorafenib. Mechanistically, treatment with **11d** upregulated pro-apoptotic markers BAX, caspase-8, and caspase-9, while downregulating the anti-apoptotic marker Bcl-2, resulting in a significant BAX/Bcl-2 ratio increase (16.11). A wound healing assay confirmed **11d**'s anti-migratory effects, limiting wound closure in MDA-MB-231 cells to 27.51% compared to untreated cells. Additionally, flow cytometry revealed that **11d** induced both early (46.43%) and late apoptosis (31.49%) in MDA-MB-231 cells, alongside G1 phase cell cycle arrest, reducing S and G2/M phase progression. Molecular docking and dynamics simulations over 200 ns demonstrated stable binding of compound **11d** to VEGFR-2, with docking scores superior and comparable to sorafenib. Density Functional Theory (DFT) calculations underscored **11d**'s stability and reactivity, while *in silico* ADMET analysis predicted a favorable safety profile over sorafenib, particularly with respect to carcinogenic and chronic toxicity risks. These findings indicate that quinoxaline derivative **11d** holds potential as a selective and effective VEGFR-2 inhibitor with promising antitumor and anti-metastatic properties, warranting further investigation.

Received 22nd January 2025
Accepted 13th April 2025

DOI: 10.1039/d5ra00526d

rsc.li/rsc-advances



## 1. Introduction

Cancer remains one of the leading causes of mortality worldwide,[1] with breast cancer being one of the most prevalent and challenging forms to treat due to its potential for metastasis and resistance to standard therapies.[2] According to the latest global cancer statistics, breast cancer accounted for approximately 2.26 million new cases in 2020 and remains the leading cause of cancer-related deaths among women globally.[3] Among the therapeutic targets in cancer treatment, vascular endothelial growth factor receptor 2 (VEGFR-2) has gained significant attention for its role in promoting angiogenesis, which supports tumor growth and metastatic spread.[4,5] Targeting VEGFR-2 with specific inhibitors can disrupt angiogenesis, thereby impeding tumor progression and offering a potential strategy for cancer management.[6,7]

Quinoxaline derivatives have emerged as promising scaffolds in anti-cancer drug development,[8] particularly in the context of breast cancer.[9] Structurally, quinoxalines offer versatile chemical frameworks that can be modified to enhance selectivity and potency toward specific molecular targets, including VEGFR-2.[10] Previous studies have shown that quinoxaline-based compounds can effectively inhibit cancer

[a]*Pharmaceutical Medicinal Chemistry & Drug Design Department, Faculty of Pharmacy (Boys), Al-Azhar University, Cairo, 11884, Egypt. E-mail: Ibrahimeissa@azhar.edu.eg; Hazemelkady@azhar.edu.eg*

[b]*Department of Medicinal Chemistry, Faculty of Pharmacy, Sana'a University, 18084 Sana'a, Yemen*

[c]*Chemistry Department, Faculty of Science, New Valley University, El-Kharja, 72511, Egypt*

[d]*Physics Department, Faculty of Science, Alexandria University, Alexandria, Egypt*

[e]*Department of Pharmaceutical Sciences, College of Pharmacy, Princess Nourah Bint Abdulrahman University, P. O. Box 84428, Riyadh 11671, Saudi Arabia*

[f]*Department of Pharmaceutical Sciences, College of Pharmacy, AlMaarefa University, P.O. Box 71666, Riyadh 11597, Saudi Arabia*

[g]*Pharmacognosy and Medicinal Plants Department, Faculty of Pharmacy (Boys), Al-Azhar University, Cairo 11884, Egypt. E-mail: ametwaly@azhar.edu.eg*

† Electronic supplementary information (ESI) available. See DOI: https://doi.org/10.1039/d5ra00526d

cell proliferation and metastasis, though further exploration is needed to optimize their efficacy and safety profiles.[11]

Building on these findings and our ongoing efforts to develop novel anticancer agents,[12–17] particularly quinoxaline derivatives,[18–22] we designed, synthesized, and evaluated a new series of quinoxaline derivatives targeting VEGFR-2 as potential anti-breast cancer agents. These compounds were designed based on key pharmacophoric features known to interact with VEGFR-2, aiming to maximize binding affinity and biological activity. Among the synthesized derivatives, compound **11d** showed particular promise, exhibiting selective cytotoxicity in cancer cells. In addition, **11d** demonstrated significant anti-migratory activity, induced apoptosis, and caused cell cycle arrest, indicating its potential as a multi-faceted anti-cancer agent.

To provide a comprehensive evaluation, we complemented our experimental findings with *in silico* analyses, including molecular docking, molecular dynamics (MD) simulations, density functional theory (DFT) studies, and ADMET profiling.

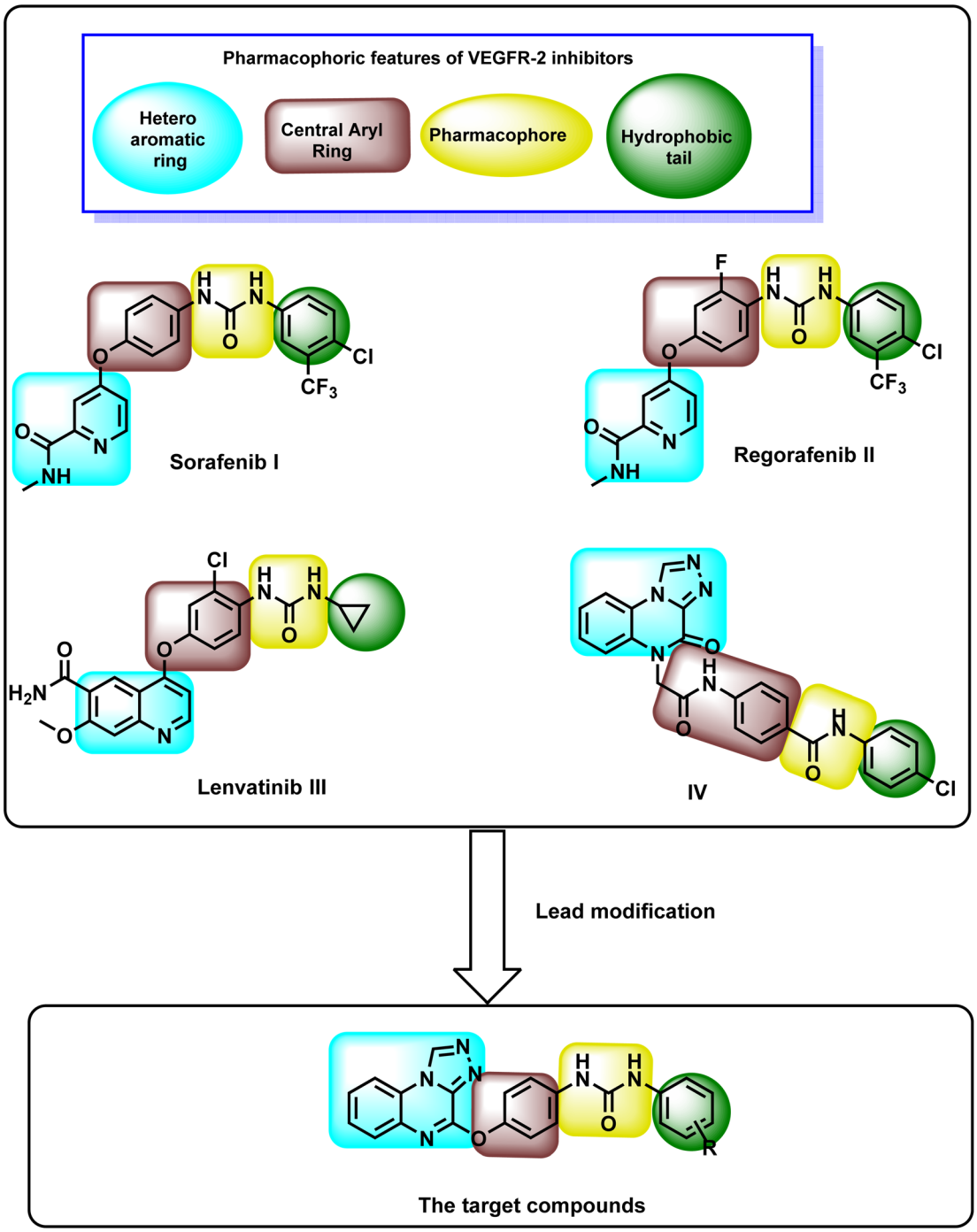


Fig. 1 Design rationale for the synthesized quinoxaline derivatives.

These computational approaches allowed us to investigate the stability, reactivity, pharmacokinetic, and toxicological properties of compound **11d**, further supporting its potential as a targeted cancer therapeutic. The promising results from this study underscore the therapeutic potential of quinoxaline derivatives in the development of new VEGFR-2 inhibitors and highlight the need for further preclinical evaluation of compound **11d** as an anti-cancer candidate.

### 1.1. Rationale

Several VEGFR-2 inhibitors have received FDA approval for the clinical treatment of cancer.[23–29] Fig. 1 shows some VEGFR-2 inhibitors as sorafenib **I**,[30,31] regorafenib **II**,[32] and lenvatinib **III**,[33] which are urea-based derivatives.[34–38] These drugs are approved for various cancers, including prostate cancer, thyroid cancer, melanoma, renal cell carcinoma, and hepatocellular carcinoma.[39,40] However, their use is often associated with adverse effects such as cardiovascular complications, diarrhea, renal impairment, fatigue, hypertension, reduced appetite, nausea, thrombocytopenia, and proteinuria.[41–45]

Our research group recently introduced compound **IV**, a bis([1,2,4]triazolo)[4,3-*a*:3′,4′-*c*]quinoxaline derivative, as a promising VEGFR-2 inhibitor with notable anti-proliferative activity against HepG-2 and MCF-7 cell lines. Compound **IV** effectively induced cell cycle arrest in HepG-2 cells at the G2/M phase and exhibited a strong pro-apoptotic effect. Additionally, it significantly increased the levels of caspase-3, caspase-9, and BAX while reducing the expression of Bcl-2 in treated cells.[46]

The chemical structure of VEGFR-2 inhibitors must include four key pharmacophoric features for effective binding at the VEGFR-2 active site (Fig. 1). (i) The first feature is a heteroaromatic moiety, essential for forming hydrogen bonds with Cys917 in the hinge region of the ATP-binding site.[47] (ii) The second is a spacer group that occupies the space between the hinge region and the DFG domain (Asp–Phe–Gly motif located in the activation loop of protein kinases, which plays a critical role in regulating kinase activity and ATP binding).[48] (iii) The third feature is a pharmacophore comprising hydrogen bond donor and acceptor groups, enabling interactions with Glu883 and Asp1044 in the DFG domain.[49] (iv) The fourth is a terminal hydrophobic moiety, which engages in hydrophobic interactions with the allosteric hydrophobic pocket of the active site.[50–52]

The rationale in this research focused on modifying compound **IV** to develop new anti-proliferative agents targeting VEGFR-2 with enhanced apoptotic potential. The newly designed compounds incorporate bis([1,2,4]triazolo)[4,3-*a*:3′,4′-*c*]quinoxaline and urea functional groups. The design strategy preserved the bis([1,2,4]triazolo)[4,3-*a*:3′,4′-*c*]quinoxaline moiety from compound **IV** as a heterocyclic core due to its established biological benefits. This moiety contains four nitrogen atoms that act as electron acceptors, facilitating hydrogen bonding in the hinge region. Additionally, its planar structure promotes hydrophobic interactions within the hinge region. Previous studies have highlighted its promising anti-proliferative activity.[53–55] The second modification line included a phenoxy group, as observed in compounds **I**, **II**, and **III**, which served as a linker. The third modification line incorporated the urea group from compounds **I**, **II**, and **III**, functioning as a pharmacophore. Lastly, various substituted aromatic groups were introduced as hydrophobic tails to explore the structure–activity relationship (Fig. 1).

## 2. Results and discussions

### 2.1. Chemistry

The chemical processes for furnishing the target molecules are shown in Scheme 1. Initially, *o*-phenylenediamine **1** reacted with oxalic acid **2** in the presence of 4 N HCl to get 2,3-(1*H*,4*H*)-quinoxalinedione **3**.[56,57] Subsequent treatment of compound **3** with thionyl chloride yielded 2,3-dichloroquinoxaline **4**. The reaction of compound **4** with hydrazine hydrate at ambient temperature yielded 2-chloro-3-hydrazinylquinoxaline **5**.[56,57] Subsequently, compound **5** was subjected to heating with triethyl orthoformate, resulting in the formation of 4-chloro [1,2,4]triazolo[4,3-*a*]quinoxaline **7**.[56,57] The subsequent step involved the reaction of isocyanate derivatives including phenyl isocyanate, 3-chlorophenyl isocyanate, 4-chlorophenyl isocyanate, and 3-methoxyphenyl isocyanate **9a–d**, respectively with *para*-aminophenol **8** in acetonitrile, resulting in the formation of the key intermediates **10a–d**.[58] Finally, a nucleophilic substitution reaction of the formed intermediates **10a–d** with compound **7** in the presence of triethylamine (TEA) in THF resulted in the synthesis of target compounds **11a–d**, respectively with commendably high yield.

Spectral data were used to describe compounds **11a–d**. These compounds' IR spectra revealed prominent NH bands at 3331–3103 $cm^{-1}$. Additionally, it had significant C=O absorption bands between 1654 and 1682 $cm^{-1}$. Moreover, the triazolo CH protons of the four derivatives were identified by singlet signals in $^1H$ NMR spectra with $\delta$ 10.13 and 10.17 ppm. These results were supported by $^{13}C$ NMR spectra, which revealed distinctive peaks for the corresponding carbons.

### 2.2. Biological evaluation

**2.2.1. Cytotoxicity and selectivity.** The *in vitro* cytotoxicity ($IC_{50}$) values of the synthesized compounds **11a**, **11b**, **11c**, and **11d** against breast cancer cell lines MDA-MB-231 and MCF-7 are summarized in Table 1, with comparisons to sorafenib. Among the tested compounds, **11d** showed the highest potency. Compound **11d** showed notable cytotoxicity in cancer cell lines, with $IC_{50}$ values of 21.68 μM in MDA-MB-231 and 35.81 μM in MCF-7, though it is less potent than sorafenib (7.64 μM and 7.26 μM, respectively).

In normal cell lines WI-38 and WISH, **11d** has significantly higher $IC_{50}$ values (82.46 μM and 75.27 μM, respectively), indicating lower toxicity compared to sorafenib, which have $IC_{50}$ values of 10.65 μM and 13.45 μM, respectively. The selectivity index (SI), calculated as the ratio of $IC_{50}$ in normal cells (WI-38 or WISH) to that in cancer cells (MDA-231 or MCF-7), highlights the preferential cytotoxicity of compounds. For sorafenib, the SI

 

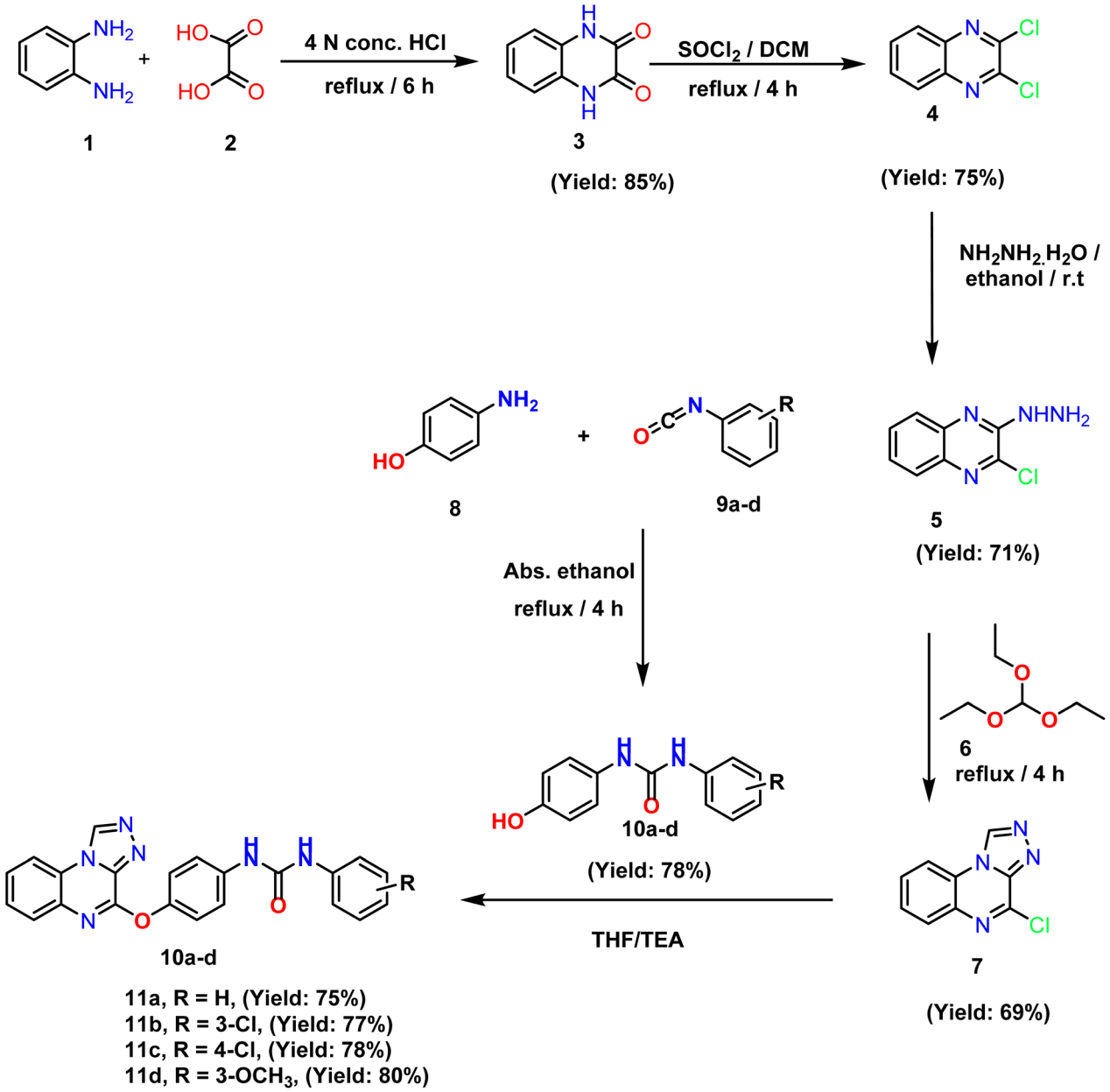


Scheme 1 Synthesis of the final compounds **11a–d**.

Table 1 *In vitro* cytotoxicity ($IC_{50}$) of **11a**, **11b**, **11c**, **11d** and sorafenib and against breast cancer and normal cell lines

| | *In vitro* cytotoxicity $IC_{50}$[a] (μM) | | | |
|---|---|---|---|---|
| Comp. | MDA-231 | MCF-7 | WI-38 | WISH |
| Sorafenib | 7.64 ± 0.4 | 7.26 ± 0.3 | 10.65 ± 0.8 | 13.45 ± 1.1 |
| **11a** | 68.40 ± 3.7 | 77.98 ± 4.1 | — | — |
| **11c** | 76.23 ± 3.9 | 69.82 ± 3.6 | — | — |
| **11d** | 21.68 ± 1.5 | 35.81 ± 2.3 | 82.46 ± 4.2 | 75.27 ± 3.9 |
| **11b** | 33.56 ± 2.1 | 46.53 ± 2.7 | — | — |

[a] The values are expressed as the mean ± SEM from three independent experiments.

ranges from 1.39 to 1.85, indicating limited selectivity between cancer and normal cells.

In contrast, compound **11d** exhibited significantly higher SI values, ranging from 3.80 to 11.29, demonstrating greater selectivity for cancer cells over normal cells. This selective cytotoxicity of **11d** suggests a promising therapeutic window, as it appears to be more effective against cancer cells than normal cells, making it a potentially safer candidate for further development.

Compound **11b** also demonstrated moderate cytotoxicity, particularly in MDA-MB-231 cells ($IC_{50}$ = 33.56 μM), while **11a** and **11c** exhibited weaker activity, with $IC_{50}$ values above 68 μM in both cell lines. These findings suggested that **11d** holds potential as a lead compound for further investigation,

Table 2 $IC_{50}$ values of **11d** and sorafenib against VEGFR-2 kinase[a]

| Comp. | VEGFR-2, $IC_{50}$ (nM) ± SEM |
|---|---|
| **11d** | 62.26 ± 2.77 |
| Sorafenib | 53.32 ± 2.52 |

[a] Values are given as mean ± SEM of three independent experiments.

particularly due to its greater cytotoxic effect compared to the other compounds in the series.

**2.2.2. VEGFR-2 inhibition.** In order to examine the design, the ability of compound **11d** to inhibited VEGFR-2 was evaluated, yielding an $IC_{50}$ of 62.26 nM ± 2.77 (Table 2). In comparison, sorafenib, a well-known VEGFR-2 inhibitor, showed a slightly lower $IC_{50}$ of 53.32 nM ± 2.52. While sorafenib exhibited marginally greater potency, the slight difference in $IC_{50}$ values suggests that **11d** is a promising candidate for further development. The low SEM value indicates consistent and reliable results, underscoring the potential for optimizing **11d** as a VEGFR-2 inhibitor.

From cytotoxicity, selectivity, and VEGFR-2 assays, was can notice that compound **11d** exhibited an $IC_{50}$ value of 62.26 nM against VEGFR-2, while sorafenib showed a slightly lower $IC_{50}$ of 53.32 nM. While this difference might seem small, its clinical relevance extends beyond mere numerical comparison.

A slight reduction in potency could necessitate a higher therapeutic dose of **11d** compared to sorafenib to achieve the same level of VEGFR-2 inhibition. However, this must be weighed against the broader therapeutic window that **11d** demonstrates, as indicated by its higher selectivity index (SI), meaning it spares normal cells more effectively than sorafenib. This could reduce the incidence of off-target toxicities, making dose escalation more feasible.

Sorafenib, while potent, is associated with several adverse effects, including hepatotoxicity, hypertension, and fatigue. The significantly lower toxicity of **11d** in normal cells (WI-38 and

Table 3 Effect of **11d** (0.5 $IC_{50}$) on migration and wound closure in MDA-231 cells after 48 hours

| Sample | Quantitative closure (%) for scratched assay after 48 h |
|---|---|
| Control (MDA-231) | 58.95 |
| Compound **11d** (11 μM) | 27.51 |

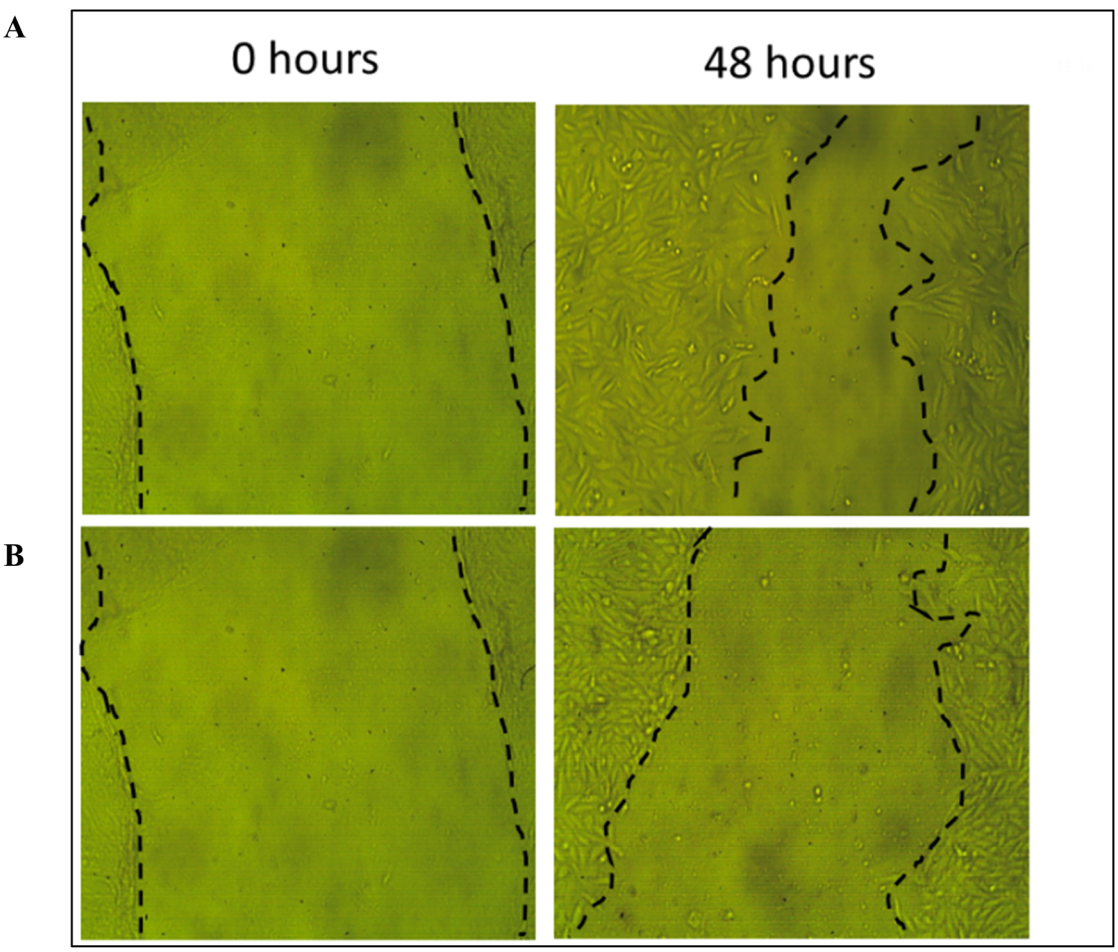


Fig. 2 Microscopic images illustrating the inhibitory effect of compound **11d** (11 μM) on the migration of the MDA-231 cell lines (B), compared to the control, untreated MDA-231 cell line, (A).

Table 4 Impact of **11d** on different stages of the cell death process in MDA-MB-231 cells following 48 h of treatment

| | | Apoptosis[b] | | |
|---|---|---|---|---|
| Sample | Viable[b] (left bottom) | Early (right bottom) | Late (right top) | Necrosis[b] (left top) |
| MDA-MB-231 | 95.48 | 3.84 | 0.45 | 0.32 |
| **11d**/MDA-MB-231 | 20.17[a] | 46.43[a] | 31.49[a] | 1.91[a] |

[a] Significant *P* value significant *P* value < 0.05 & by using one-way ANOVA followed by Tukey's *post hoc* multiple comparison tests. [b] Values represent stages of the cell death process in MDA-MB-231cells treated with or without **11d**.

WISH, $IC_{50}$ = 82.46 μM and 75.27 μM, respectively) compared to sorafenib ($IC_{50}$ = 10.65 μM and 13.45 μM) suggests that even if a slightly higher dose of **11d** is required for equivalent VEGFR-2 inhibition, it may still offer a superior safety profile.

The balance between potency and selectivity is critical for drug development. Although **11d**'s $IC_{50}$ is slightly higher than sorafenib's, its higher selectivity and reduced toxicity could make it a preferable candidate for long-term therapy, especially in patients susceptible to sorafenib's side effects. Additionally, further formulation strategies (*e.g.*, prodrugs, nano-formulations) could enhance **11d**'s bioavailability and therapeutic efficacy, mitigating the impact of its slightly higher $IC_{50}$.

**2.2.3. Cancer cells migration and healing assay.** The cancer cell healing assay was used to evaluate the migratory potential of MDA-231 cells, providing insights into the **11d**'s ability to inhibit cell migration, a key process in metastasis (Fig. 2). In this assay, a "wound" is created in a confluent monolayer of cells, and the closure of the wound over time is measured as an indicator of cell migration. The results of this assay for compound **11d** demonstrate its anti-migratory potential in MDA-231 cells at its 0.5 $IC_{50}$ concentration. After 48 hours of treatment, as shown in Table 3, untreated cells showed a wound closure of 58.95%, reflecting typical cell migration activity. However, treatment with **11d** reduced wound closure to 27.51%, indicating a significant inhibition of migration and suggesting that **11d** interferes with the cells' ability to move across the wound area. These results highlight the compound's potential as an anti-metastatic agent.

**2.2.4. Apoptosis assay.** The data in Table 4 and Fig. 3 provide insights into the effects of compound **11d** on cell viability and stages of cell death in MDA-MB-231 cells after 48 hours of treatment, compared with untreated cells. Treatment with compound **11d** resulted in a significant reduction in viable MDA-MB-231 cells, with only 20.17% of cells remaining viable compared to 95.48% in the untreated control. Regarding apoptosis, compound **11d** induced a notable increase in apoptotic cell populations. Early apoptosis was observed in 46.43% of cells treated with **11d**. Late apoptosis was also induced at a high level (31.49%) by **11d**. These findings indicate that **11d** effectively promotes apoptotic cell death, with a substantial proportion of cells progressing to later stages of apoptosis. It's worthy to mention that minimal necrosis was

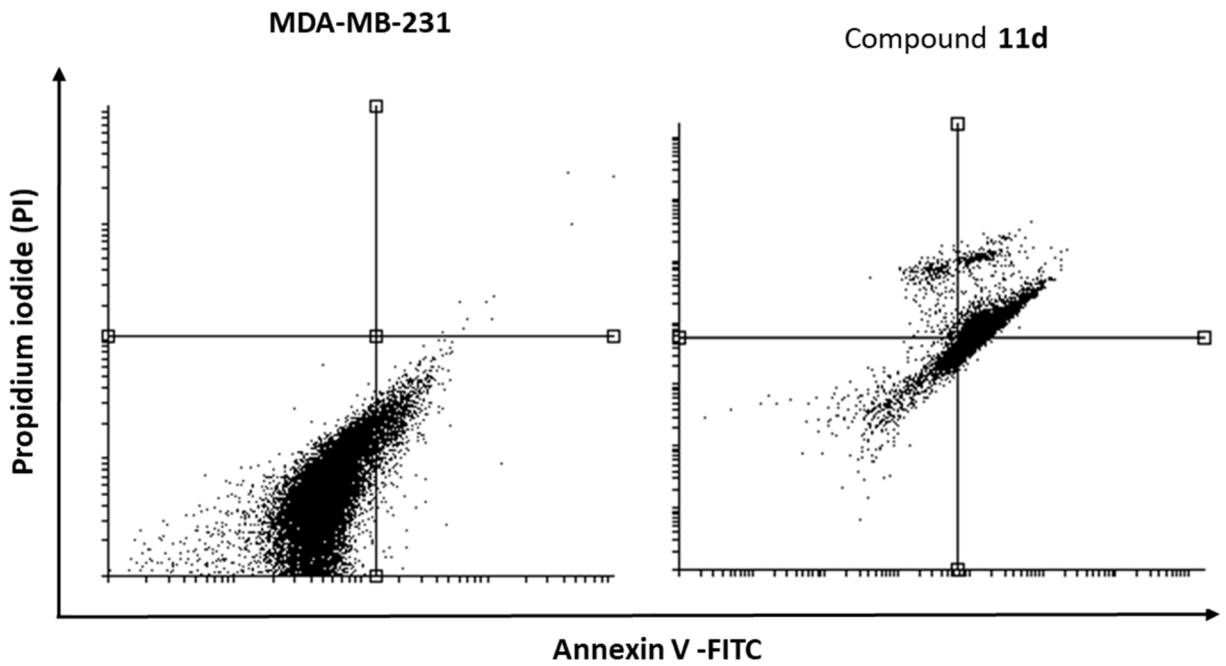


Fig. 3 The effect of compound **11d** on the cell viability of the MDA-231 cell lines.

Table 5 Impact of **11d** on cell cycle progression in MDA-MB-231 cells after 48 h of treatment

| | Cell cycle distribution[b] (%) | | | |
|---|---|---|---|---|
| Sample | % sub-G1 | % G1 | % S | % G2/M |
| MDA-MB-231 | 19.48 | 44.98 | 24.95 | 10.59 |
| **11d**/MDA-MB-231 | 15.75 | 64.06[a] | 16.45[a] | 3.74[a] |

[a] Significant *P* value significant *P* value < 0.05 & by using one-way ANOVA followed by Tukey's *post hoc* multiple comparison tests. [b] Cell cycle distribution (%) of MDA-MB-231 cells were treated with or without compound **11d**.

observed in both treated groups, with **11d** causing necrosis in only 1.91% of cells. The low levels of necrosis suggest that the primary mechanism of cell death induced by **11d** is apoptotic rather than necrotic, which is often preferable in cancer treatment to avoid inflammatory responses associated with necrosis.

**2.2.5. MDA-MB-231 cell cycle analysis.** MDA-MB-231 cell cycle analysis after **11d** treatment (Table 5 and Fig. 4) indicated that compound **11d** primarily inducing G1 phase arrest, with 64.06% of cells in the G1 phase after 48 hours, compared to 44.98% in untreated cells. This shift limited progression into the S and G2/M phases, as seen in the lower S phase (16.45%) and G2/M phase (3.74%) populations, which suggests compound **11d** effectively halts cell cycle advancement. Furthermore, compound **11d** showed a lower sub-G1 population (15.75%) compared to the untreated cells (19.48%). Overall, compound **11d**'s ability to arrest cells in G1 may offer an alternative pathway to reduce cell proliferation in cancer treatment, warranting further investigation.

**2.2.6. Quantitative reverse transcription-polymerase chain reaction (qRT-PCR) analysis.** The mRNA expression levels of apoptosis-related genes, including BAX, Bcl-2, caspase-8, and caspase-9, were analyzed in control and compound **11d**-treated MDA-231 cells (21.68 μM) using qRT-PCR. Treatment with **11d** (Table 6) significantly increased the expression of pro-apoptotic genes BAX, caspase-8, and caspase-9, with fold changes of 5.48, 4.15, and 5.58, respectively, as well as a notable decrease in anti-apoptotic Bcl-2 expression (0.34). This led to a marked increase in the BAX/Bcl-2 ratio (16.11), a strong indicator of apoptotic potential. In comparison, sorafenib also upregulated BAX and caspases but to a lesser extent, with a BAX/Bcl-2 ratio of 6.10. These results suggest that **11d** induced a more pronounced pro-

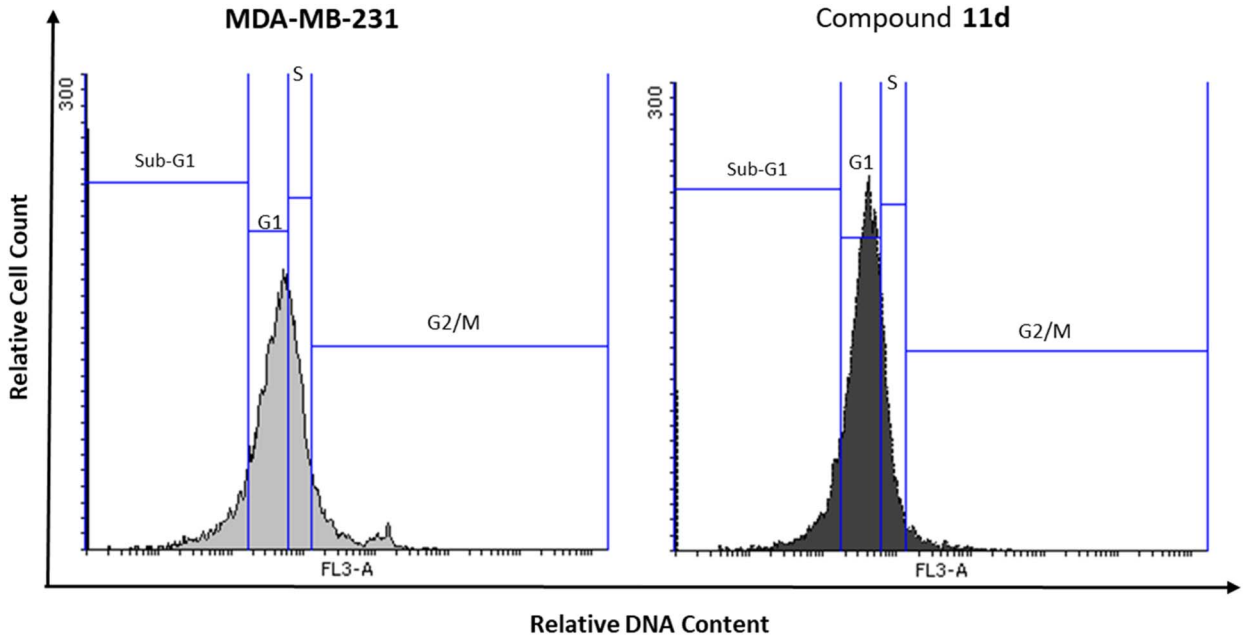


Fig. 4 Impact of compound **11d** on cell cycle progression in MDA-MB-231 cells following 48 hour treatment.

Table 6 Effect of compound **11d** (21.68 μM) on levels of BAX, Bcl-2, caspase-8, and caspase-9 genes expression in MDA-231 cells

| | Gene expression (fold change)[b] | | | | |
|---|---|---|---|---|---|
| Sample | BAX | Bcl-2 | BAX/Bcl-2 ratio | Caspases-8 | Caspases-9 |
| MDA-231 cells | 1.00 ± 0.08 | 1.00 ± 0.07 | 1.00 ± 0.13 | 1.00 ± 0.09 | 1.00 ± 0.11 |
| **11d** | 5.48 ± 0.45[a] | 0.34 ± 0.01[a] | 16.11 ± 1.01 | 4.15 ± 0.48[a] | 5.58 ± 0.40[a] |

[a] Significant *P* value significant *P* value < 0.05 & by using one-way ANOVA followed by Tukey's *post hoc* multiple comparison tests. [b] Values are given as changes from the corresponding control (MDA-231 cells) group. Data from three independent experiments represent the mean ± SEM, as the fold changes, with control is set to '1'.

apoptotic response, highlighting its potential as a promising therapeutic candidate for apoptosis induction in MDA-231 cells.

**2.2.7. Statistical analysis section.** GraphPad Prism 6 software (GraphPad, San Diego, CA, USA) was used to analyze all results. The data were represented as mean ± standard deviation (mean ± SD) from at least three independent experiments ($n = 3$). One-way analysis of variance (one-way ANOVA) followed by Tukey *post hoc* multiple comparison tests were elected to analyze the significant difference between all groups. $P < 0.05$ was considered statistically significant.

## 2.3. Computational evaluations

**2.3.1. Molecular docking study.** To further understand the biological activity of the newly synthesized derivatives (**11a–d**) and their binding interactions at the molecular level, docking simulations were conducted. The re-docking of the native

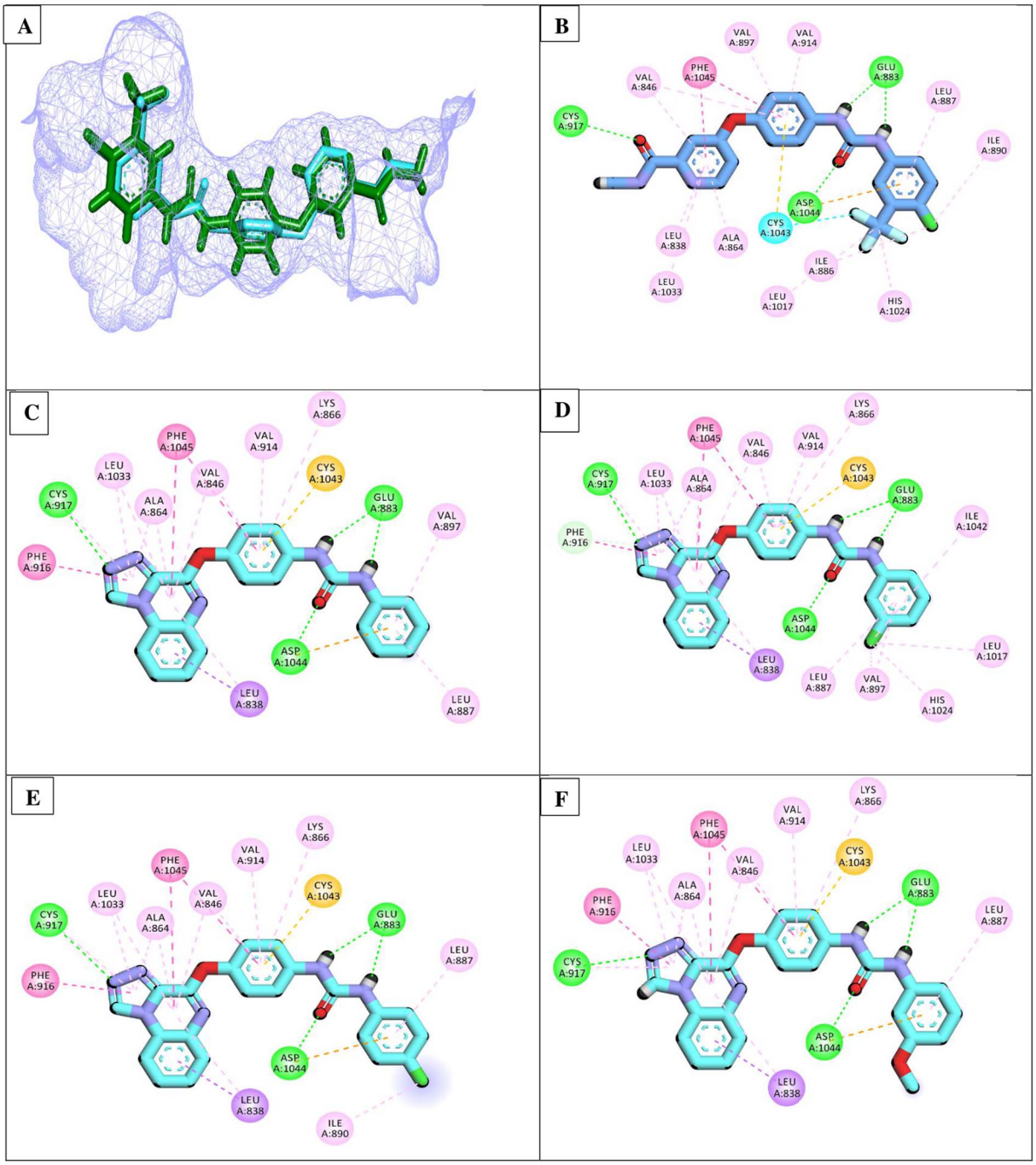


Fig. 5 (A) Overlay of the co-crystallized ligand (green) and the redocked ligand (turquoise) in the VEGFR-2 active site. 2D interaction of (B) sorafenib, (C) **11a**, (D) **11b**, (E) **11c**, and (F) **11d**, against VEGFR-2.

Table 7 The S score values for the reference inhibitor (sorafenib) against the novel compounds **11a–d**

| Comp. | **11a** | **11b** | **11c** | **11d** | Sorafenib |
|---|---|---|---|---|---|
| Energy score (kcal $mol^{-1}$) | −22.98 | −23.02 | −22.71 | −23.65 | −22.50 |

ligand at the active site of VEGFR-2 has conclusively validated the docking procedure. The results indicated a significant overlap between the native and docked ligands, with an RMSD of 0.89 Å, as illustrated in Fig. 5A.

The docking simulations evaluated the compounds' ability to interact with the active site of VEGFR-2. The docking scores for derivatives **11a–d** ranged from −22.71 to −23.65 kcal $mol^{-1}$, indicating strong binding affinities (Table 7). Notably, these scores were comparable and higher than those of sorafenib, a known VEGFR-2 inhibitor, suggesting that the new derivatives may exhibit enhanced binding efficiency. The binding score of sorafenib was determined to be −22.50 kcal $mol^{-1}$. An examination of sorafenib's binding pattern indicated alignment with the reported findings, where the hydrophobic moiety (3 chloro-4-trifluoromethylphenyl) was positioned within the allosteric site. Additionally, two significant hydrogen bonds were identified between the urea linker and Glu883 and Asp1044. Also, Cys917 forms two hydrogen bonds with the *N*-methylpicolinamide arm (see Fig. 5B).

The docking results showed that the four synthesized derivatives nearly matched the orientation and position of sorafenib in the active binding region of the VEGFR-2 enzyme (Fig. 5). The derivatives' amide groups maintained two necessary hydrogen bonds with Glu883 and Asp1044 in the DFG domain. Interestingly, the hydrophobic moieties of the synthesized candidates (phenyl, 3-chlorophenyl, 4-chlorophenyl, and 3-methoxyphenyl) behaved similarly to sorafenib and occupied the VEGFR-2 enzyme's allosteric site. Such hydrophobic moieties formed several hydrophobic bonds with Leu886, Leu887, Leu1017, and Ile890. Additionally, in the hinge area, the [1,2,4]triazolo[4,3-*a*]quinoxaline moiety of compounds **11a–d** established a crucial hydrogen bond with Cys917 and shared a number of hydrophobic contacts with Ala864, Leu1033, Phe1045, and Phe916. Moreover, the central phenyl group of the synthesized derivatives formed several hydrophobic interactions with Val846, Val914, and Lys866 besides one electrostatic interaction with Cys1043 (Fig. 5C–F).

Molecular docking results indicate that **11d** has a docking score of −23.65 kcal $mol^{-1}$, which is slightly better than sorafenib (−22.50 kcal $mol^{-1}$), suggesting a strong binding affinity for VEGFR-2. However, a deeper structural comparison with other VEGFR-2 inhibitors will enhance our understanding of its potential advantages.

*2.3.1.1. Key binding interactions.* Compound **11d** interacts with Cys917 (hinge region), Glu883 and Asp1044 (DFG domain), and Leu886, Leu887, and Ile890 (hydrophobic pocket). These interactions mirror those of known VEGFR-2 inhibitors like sorafenib and lenvatinib, reinforcing the rationale for its design.

This good binding mode is attributed to the high number of hydrophobic interaction caused by the planar bis([1,2,4]triazolo)[4,3-*a*:3′,4′-*c*]quinoxaline moiety. This moiety contains four nitrogen atoms that act as electron acceptors, facilitating hydrogen bonding in the hinge region. Additionally, its planar structure promoted hydrophobic interactions within the hinge region.

**2.3.2. MD simulations studies.** MD simulations revealed distinct differences in the dynamics of VEGFR-2 upon binding **11d** compared to sorafenib before 50 ns the VEGFR-2 backbone in the VEGFR-2_sorafenib complex (dark green line) (Fig. 6A) maintained stable RMSD values around 2 Å and VEGFR-2 backbone in the VEGFR-2_**11d** complex (red line) (Fig. 6A) maintained stable RMSD values around 4 Å. Throughout the simulation VEGFR-2 in the VEGFR-2_**11d** complex (red line) decreased to 3 Å and returned increase after 150 ns to 4 Å until the end of simulation. In contrast, VEGFR-2_sorafenib displayed a similar trend until initially but exhibited an RMSD increase after 80 ns, stabilizing around 3 Å for the remainder of the simulation. Ligand RMSD profiles (Fig. 6B) suggest stable binding in both systems. **11d** (red) displayed a stable average 2.5 Å. Also, sorafenib showed a stable RMSD throughout the whole simulation with an average of 1.5 Å. Compound **11d**'s RMSD profile (Fig. 6B) displayed stable binding in both systems. Average RoG and SASA values (Fig. 6C and D) indicated no significant changes in the protein's overall structure. However, hydrogen bond analysis (Fig. 6E) revealed distinct interaction patterns. Sorafenib formed a relatively constant two hydrogen bond throughout the simulation, with a small number of frames showing three H-bonds. **11d**, on the other hand, exhibited an increased number of frames with three H-bonds hydrogen bond analysis (Fig. 6E) revealed that the complex formed a relatively constant four hydrogen bonds throughout the simulation, with a few frames showing three H-bonds. RMSF profiles of C-alpha atoms (Fig. 6F) showed nearly identical fluctuations for both systems except for the LYS995 and LYS1060 displayed higher RMSF in the VEGFR-2_**11d** system compared to the reference system. LYS995 (up to 4.9 Å) and LYS1060 (maximum 7.68 Å), reflecting their increased mobility associated with LYS1060 is close to the next residue ASP110 at the end of the simulation. The center-of-mass distance analysis (Fig. 6G) indicated stable ligand binding in both systems. **11d** maintained a slightly higher average distance (up to 9 Å) compared to sorafenib (up to 8 Å). Overall, these findings suggest that both systems retain overall structural stability. The ligands exhibit distinct binding dynamics, with **11d** showing more flexibility compared to the tighter interactions of sorafenib.

**2.3.3. MM-GBSA analysis.** Fig. 7 unveils the intricate components of the predicted binding free energies calculated using the MM-GBSA method. Despite exhibiting a slightly lower overall binding affinity (−43.3 kcal $mol^{-1}$) compared to sorafenib (−51.3 kcal $mol^{-1}$), **11d** demonstrates interesting

 

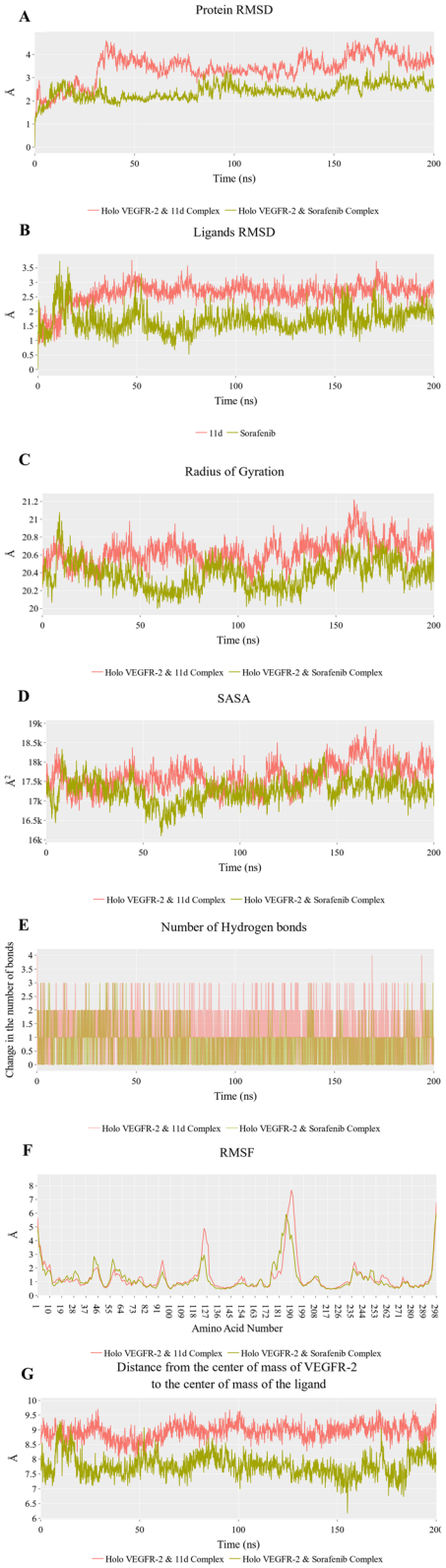


Fig. 6 MD analysis parameters: (A) RMSD values from the trajectory for the VEGFR-2 protein in VEGFR-2_**11d** (red line) and VEGFR-2_sorafenib complex (dark green line), (B) shows the ligands RMSD values, (C) radius of gyration for the VEGFR-2 protein in VEGFR-2_**11d** (red line) and VEGFR-2_sorafenib complex (dark green line), (D) SASA for VEGFR-2 protein in VEGFR-2_**11d** (red line) and VEGFR-2_sorafenib complex (dark green line), (E) change in the number of hydrogen bonds between **11d** (pink line) or sorafenib (brown line) and VEGFR-2, (F) RMSF for VEGFR-2 protein in VEGFR-2_**11d** (red line) and VEGFR-2_sorafenib complex (dark green line), (G) distance from the center of mass of sorafenib or **11d** compound and VEGFR-2 protein.

similarities and dissimilarities in its interaction profile. Both ligands benefit from robust van der Waals interactions averaging around −53 kcal $mol^{-1}$. However, when considering electrostatic contributions, **11d** shows a significantly more favorable electrostatic term (−21.16 kcal $mol^{-1}$) compared to sorafenib (−8.9 kcal $mol^{-1}$). To pinpoint the contribution of amino acid residues within 1 nm of each ligand, decomposition analysis was performed (Fig. 8). Interestingly, twelve residues exhibit enhanced contributions to **11d** binding compared to sorafenib. These key amino acids are Leu838 (−1.5 kcal $mol^{-1}$ for **11d** *vs.* −1.3 kcal $mol^{-1}$ for sorafenib), Val 846 (−1.07 kcal $mol^{-1}$ for **11d** *vs.* −1.2 kcal $mol^{-1}$ for sorafenib), Ala864 (−1.09 kcal $mol^{-1}$), Leu887 (−1.5 kcal $mol^{-1}$ for **11d** *vs.* −1.59 kcal $mol^{-1}$ for sorafenib), Val897 (−1.35 kcal $mol^{-1}$ for **11d** *vs.* −1.06 kcal $mol^{-1}$ for sorafenib), Val914 (−1.5 kcal $mol^{-1}$ for **11d** *vs.* −1.2 kcal $mol^{-1}$ for sorafenib), Phe916 (−2,5 kcal $mol^{-1}$ for **11d** *vs.* −1 kcal $mol^{-1}$ for sorafenib), Cys917 (−2.2 kcal $mol^{-1}$ for **11d**), Leu1033 (−1.6 kcal $mol^{-1}$ for **11d** *vs.* −1.2 kcal $mol^{-1}$ for sorafenib), Cys1043 (−3 kcal $mol^{-1}$ for **11d** *vs.* −2.3 kcal $mol^{-1}$ for sorafenib), Asp1044 (−1.6 kcal $mol^{-1}$ for **11d** *vs.* −1.9 kcal $mol^{-1}$ for sorafenib), Phe1045 (−1.1 kcal $mol^{-1}$ for sorafenib).

**2.3.4. Protein–ligand interaction fingerprint (ProLIF) analysis.** Protein–Ligand Interaction Fingerprints (ProLIF) analysis shed light on the specific amino acids involved in ligand interactions within the VEGFR-2 binding pocket. Fig. 9A–C and 10 represent amino acids that exhibited a high propensity for hydrophobic interactions (H.I.), van der Waals (VdW) contact, and hydrogen bond acceptor (HBA) with a ratio of >80% occurrence, respectively. For **11d** (Fig. 9) these key amino acids are LEU (98%, H.I.), VAL846 (99.5%, H.I.), ALA864 (99.5%, H.I.), LYS866 (91%, H.I.), GLU883 (84%) H.I., ILE886 (90.3%) H.I., LEU887 (98.3% H.I.), VAL897 (89.2% H.I.), VAL914 (99.9% H.I.), GLU915(98.6%, VdW), and (97.4%, HBD), PHE916 (90.4%, H.I.), CYS917 (98.7%, VdW), and (92%, HBA), LEU1033 (99.8%, H.I.), CYS1043 (94.4%, H.I.), ASP1044 (93.8%, H.I.), (99.9%, VdW) and (99%, HBA). In contrast, For sorafenib (Fig. 10) 13 amino acids exhibited a high propensity for hydrophobic interactions (>80% occurrence). Key amino acids are Leu838 (91.2%), Val846 (98.6%), Lys866 (87.9%), Ile886 (92.9%), Leu887 (95.1%), Ile890 (95.2%), Val897 (88.9%), Val914 (99.7%), Leu1017 (95.4%), His1024 (86.6%), Leu1033 (91%), Cys1043 (99.8%), and Asp1044 (99.3%). Furthermore, Asp1044 contributed *via* hydrogen bonding, with a formation rate of 88.2%.

**2.3.5. Essential dynamics.** Principal Component Analysis (PCA) was our preferred technique for determining the coordinates of the α-carbon atoms in the VEGFR-2 complex. The right dimensions of the reduced subspace must be carefully determined taking into account a number of the parameters mentioned in the ESI Methods section.† Among them was the cumulative variation that could be accounted for by a larger

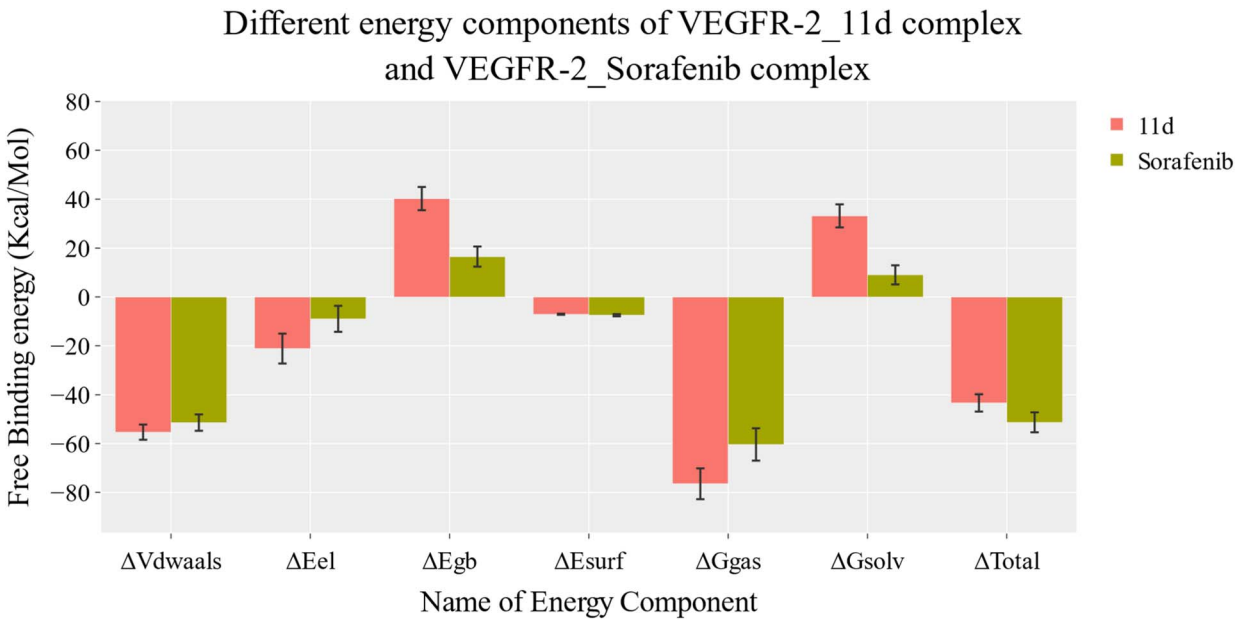


Fig. 7 MM-GBSA analysis of the VEGFR-2-**11d** complex and VEGFR-2-sorafenib complex. Bars represent the standard deviations.

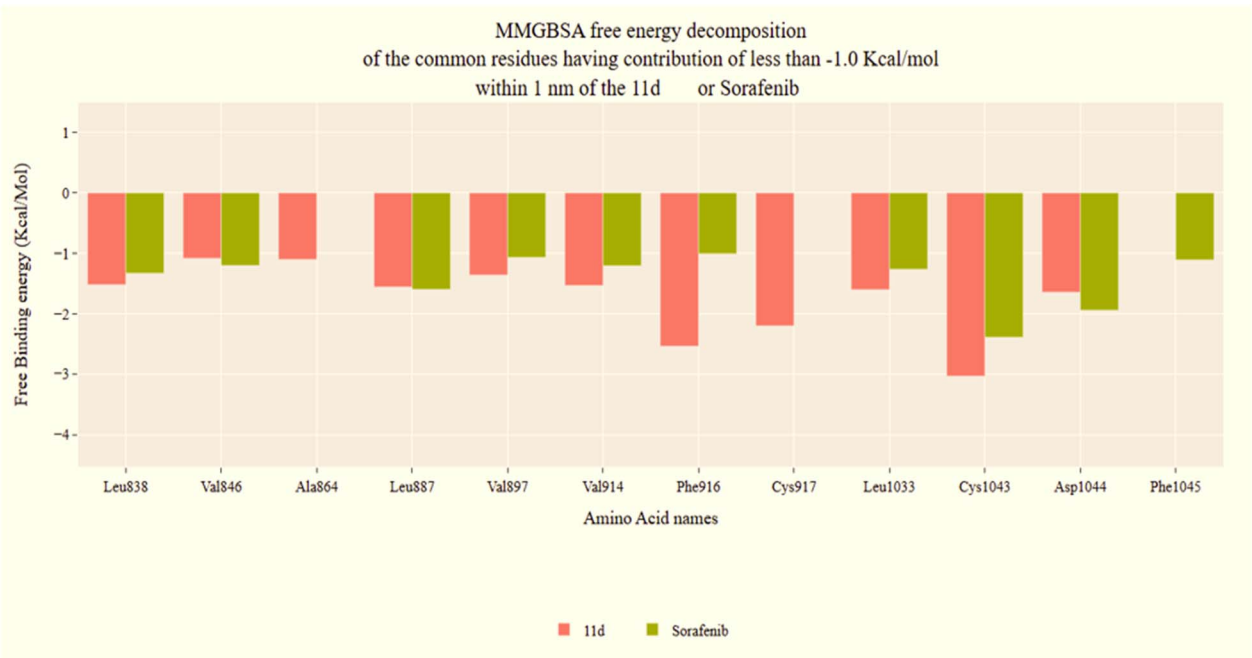


Fig. 8 VEGFR-2-**11d** complex and VEGFR-2-sorafenib complex binding free energy decomposition.

number of principal components (PCs), the scree plot, and the eigenvector distribution. The scree plot (Fig. 11A) showed that the slope began to significantly reduce at the third PC, indicating a possible point of inflection for the selection of dimensionality. As seen in Fig. 11A, the first eigenvector alone accounted for a significant 76.17% of the overall variance, while the first three PCs combined contributed roughly 86.24%. This suggested that these three PCs accounted for a sizable fraction of the total protein movements. The distributions of the first five PCs differed from the Gaussian distribution, which further supported this decision (Fig. 11B). A non-Gaussian distribution often indicates significant, non-random motions that these components can capture. Accordingly, we selected the top five PCs to illustrate the essential subspace using a combination of non-Gaussian eigenvector distributions, variance collected, and scree plot. We then examined the Root Mean Square Inner Product (RMSIP) and cosine content of the complex's first 10 principal components (PCs) to assess any potential redundancy and unpredictability within the indicated key subspaces. We subsequently examined the cosine content of the first ten principal components (PCs) for

 

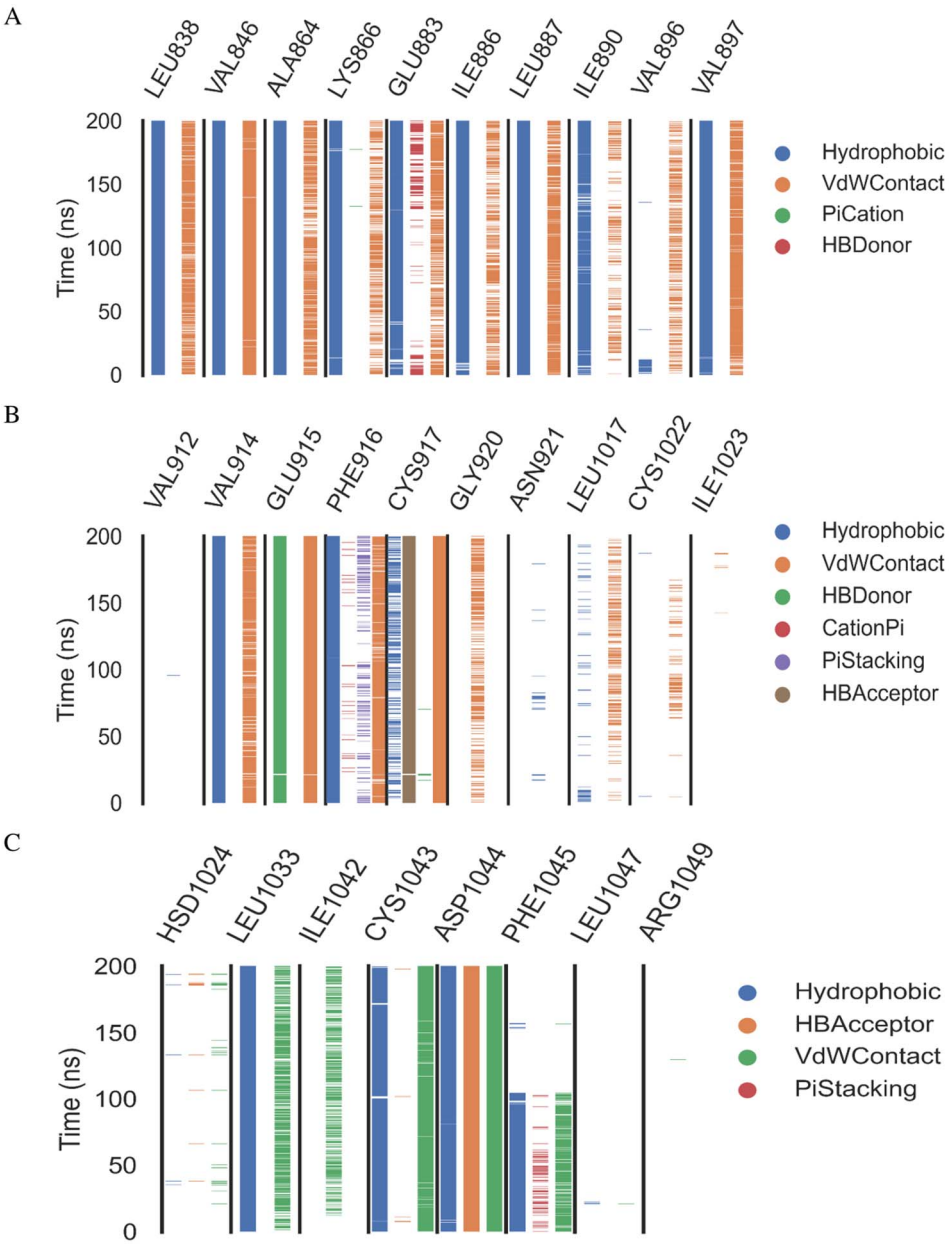


Fig. 9 ProLIF assay: the ProLIF Python library was used to analyze the amino acids involved, the types of interactions within compound **11d**-VEGFR-2 complex, and their frequency throughout the entire simulation. Panel (A) represents hydrophobic interactions (H.I.), panel (B) depicts van der Waals (VdW) contacts, and panel (C) shows hydrogen bond acceptor (HBA) interactions.

the VEGFR-2 system (Fig. 11C). Except for the second PCs (0.23 for VEGFR-2_sorafenib and 0.45 for VEGFR-2_**11d**) and the third PC of VEGFR-2_**11d** (0.10), all other cosine values for the first ten PCs remained below 0.2. This suggests that the identified essential motions captured by the PCs are not random. The RMSIP analysis indicated limited overlap between the two covariance matrices. Focusing on the initial three PCs, which capture the most significant variance, the RMSIP value was only 23.9%. This low value implies that the dominant collective motions represented by these initial PCs are largely non-overlapping between the two systems. Additionally, the overall RMSIP analysis revealed that the C matrices, encompassing the complete set of eigenvectors, were only 35% similar. This underscores the distinct sampling characteristics and dynamic landscapes experienced by VEGFR-2 in each complex.

**2.3.6. Free energy landscape (FEL) analysis.** The projected trajectories onto various two-dimensional planes defined by the chosen PCs are displayed in Fig. 12. Every graphic displays a different landscape with different basins that correspond to local minima on the FEL. These basins correspond to preferred conformations adopted by the protein–ligand complex during the simulation. For the projection on the first two PCs (Fig. 12A), the sampling starts from (white dots) basin and then moves to a transient basin (white and grey dots) before finally reaching the most stable one (black dots). There is a 2.090 kJ $mol^{-1}$ difference between the global minimum and the next minimum. Fig. 12B

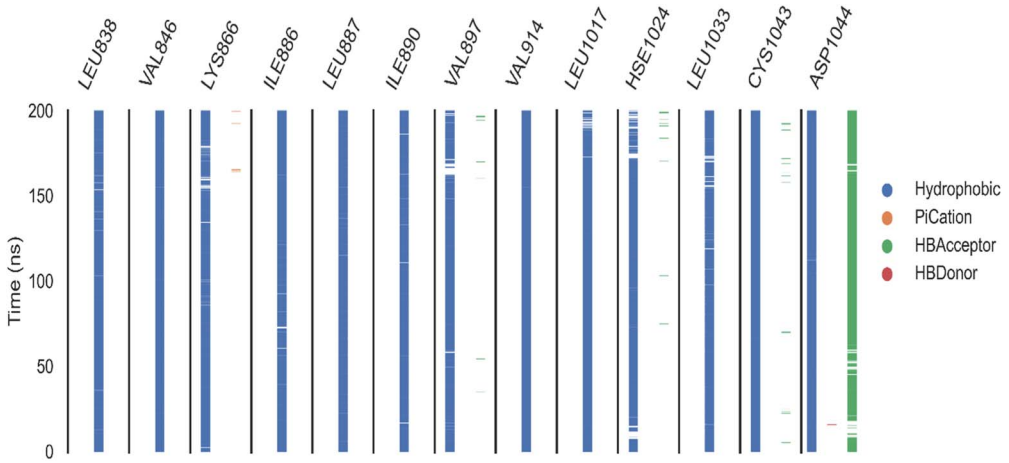


Fig. 10 ProLIF assay: the ProLIF Python library was used to analyze the amino acids involved, the types of interactions within compound sorafenib-VEGFR-2 complex, and their frequency throughout the entire simulation.

presents the projection on PC1–PC3, which shows a projection with three basins, the trajectories move from the transient basin in the middle (white dots) to the stable basin (white grey and dark dots). The difference in energy between the global and the next minima is calculated to be 0.27 kJ $mol^{-1}$. Similarly, Fig. 12C shows the projection on PC2 and PC3, revealing a wide basin and a narrow basin. The trajectory begins in the wide basin and then transitions to the narrow basins (the most stable basin) at the end of the simulation (black dots). The difference between the second and global minima is 0.0 kJ $mol^{-1}$.

**2.3.7. Density functional theory (DFT) calculations.** DFT calculations for compound **11d** were carried out using Gaussian 09 software with the 6-31+G(d, p) basis set to investigate its stability, reactivity, and electrical properties following its structural optimization. Under the same theoretical framework, the quantum investigations of global reactivity, energy gap ($E_{gap}$) and molecular electrostatic surface potential (MESP) were also carried out. In Fig. 13A, the optimized structure of **11d** is shown. Following the optimization process, Table 8's computed dipole moment ($D_m$) value (7.301 debye) was comparatively high. A higher degree of dipole moment corresponds to a larger degree of charge separation in **11d**, so the $D_m$ value is used as an indicator of charge separation in **11d**. Since dipole–dipole interactions are common among molecules with strong dipole moments, a higher DM value indicates a polar molecule and can provide information about its reactivity. These interactions can impact a molecule's reactivity in polar liquids.[59]

As seen in Fig. 13B, the density of the LUMO function is mostly dispersed across **11d**'s right side, but the distribution of the HOMO function is virtually evenly distributed over the left side. This unique distribution raises the possibility that directionality in the electron transfer routes through **11d** from HOMO to LUMO which is important in electron transfer and charge separation reactions which are relevant in drug interaction. Additionally, as the HOMO designates the area where an electron can be transferred, the target will be able to approach the right side of **11d** electrophilically. It was discovered that the HOMO/LUMO energy gap ($E_{gap}$) was 3.569 eV. Table 8 displays the calculated global reactivity parameters. The electrophilicity index of **11d** was determined to be 15.142 eV, indicating that it has a high electron-accepting capacity from biomolecules. Due to its high electrophilicity, the medication may interact effectively with protein nucleophilic sites. Also, **11d** is soft (0.560 eV). The electrons' ability to escape is measured by chemical potential, which was found to be −4.12 eV. When a molecule loses electrons, its chemical potential is negative, indicating that it is relatively stable. A molecule is less able to donate electrons when its negative chemical potential is higher, which makes it more difficult to oxidize.[60]

To identify the nucleophilic and electrophilic active sites, Fig. 13C presents the analysis and presentation of the molecular electrostatic potential, or MESP. The electron-rich site's negative potential, as indicated by the MESP map, can form hydrogen bonds with the target's electrophilic active sites by spreading over the C=O groups. The blue zones on hydrogens indicate sites that are electron-deficient have the ability to make hydrogen bonds with the target's nucleophilic sites. The target protein's hydrophobic regions can interact with the neutral green patches on the MESP map, Fig. 13C.

The overall density of states was examined using Multiwfn software, along with the number of states that might be created at each level. The HOMO energy line is shown as a dashed line in Fig. 13D. The electronic density of states is larger for orbitals higher than the LUMO, as can be seen from the total density chart. This suggests that **11d** can readily receive more electrons from electron donors in biological settings. Because of its capacity to take electrons, **11d** is more reactive in oxidative stress conditions, which are frequently present in cancer cells.

**2.3.8. *In silico* ADMET analysis.** To evaluate the pharmacokinetic profile of the synthesized compounds, Table 9 presents a summary of key properties for compounds **11a–d**, including blood–brain barrier (BBB) permeability, solubility, absorption, CYP2D6 inhibition, and plasma protein binding (PPB), alongside sorafenib. Among the compounds, only **11a** exhibited high BBB permeability, indicating potential central nervous system (CNS) activity, which could be advantageous or a limitation depending

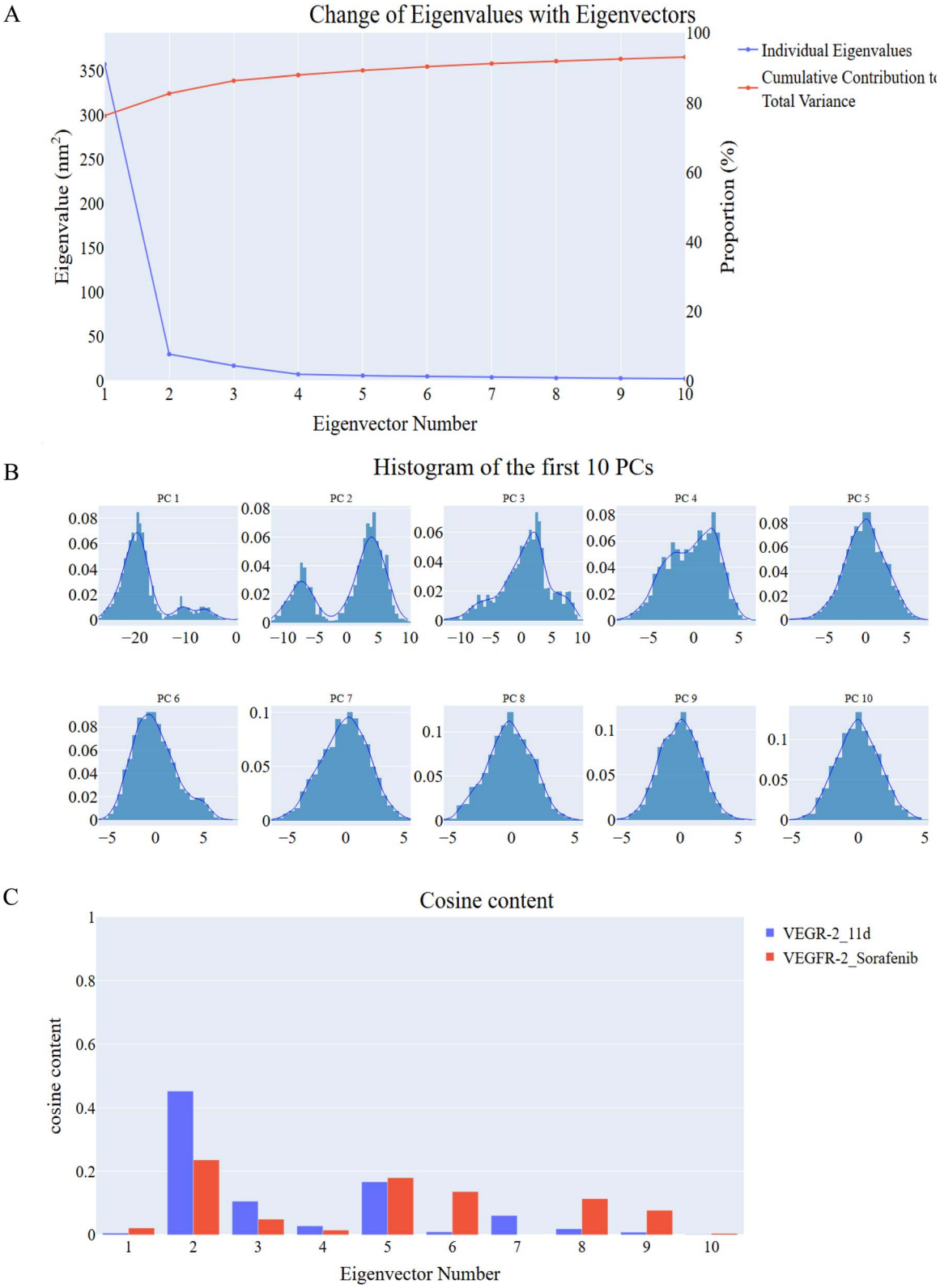


Fig. 11 Essential dynamics analysis for the first ten eigenvectors of VEGFER-2-**11d** complex and VEGFER-2-sorafenib complex. (A) Eigenvalues changing, (B) the eigenvectors' distribution, and (C) cosine values.

on the therapeutic application. The remaining compounds, including sorafenib, show very low BBB permeability, suggesting limited CNS exposure, which may reduce the risk of CNS-related side effects. Solubility remains a challenge, as compounds **11b**, **11c**, and sorafenib exhibited very low solubility, while **11a** and **11d** showed slightly improved but still low solubility. Despite these solubility limitations, all compounds demonstrate good absorption levels, potentially supporting sufficient bioavailability for

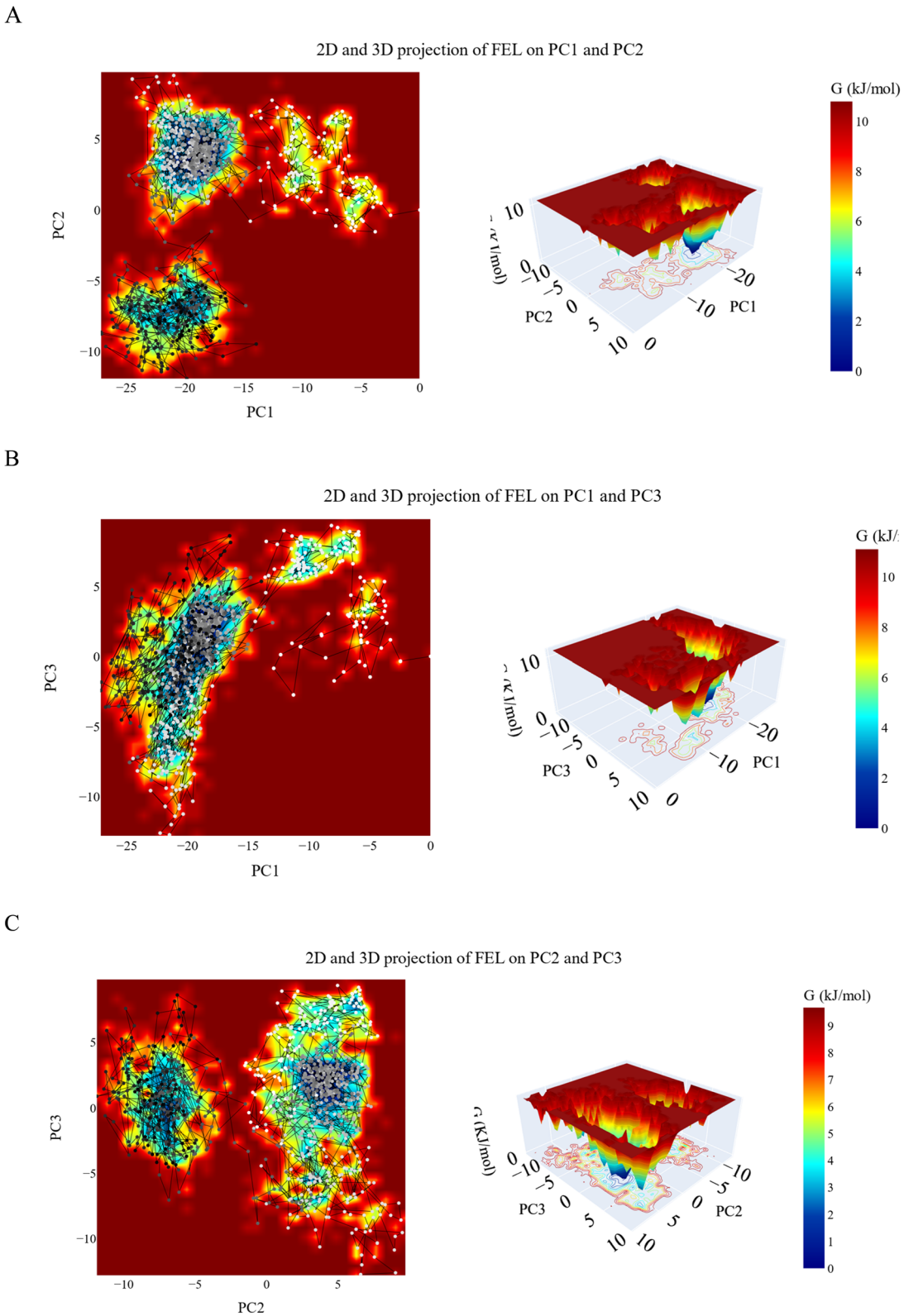


Fig. 12 The 2D and 3D projections of the VEGFR-2_**11d** complex trajectories FEL on (A) the first two, (B) first and third and (C) second and third eigenvectors.

systemic action. In terms of metabolic interaction, all compounds are predicted to be non-inhibitors of CYP2D6, reducing the risk of drug–drug interactions *via* this pathway. Furthermore, each compound has a PPB prediction greater than 90%, indicating high plasma protein binding, which could impact distribution and bioavailability. Overall, the good absorption and non-CYP2D6

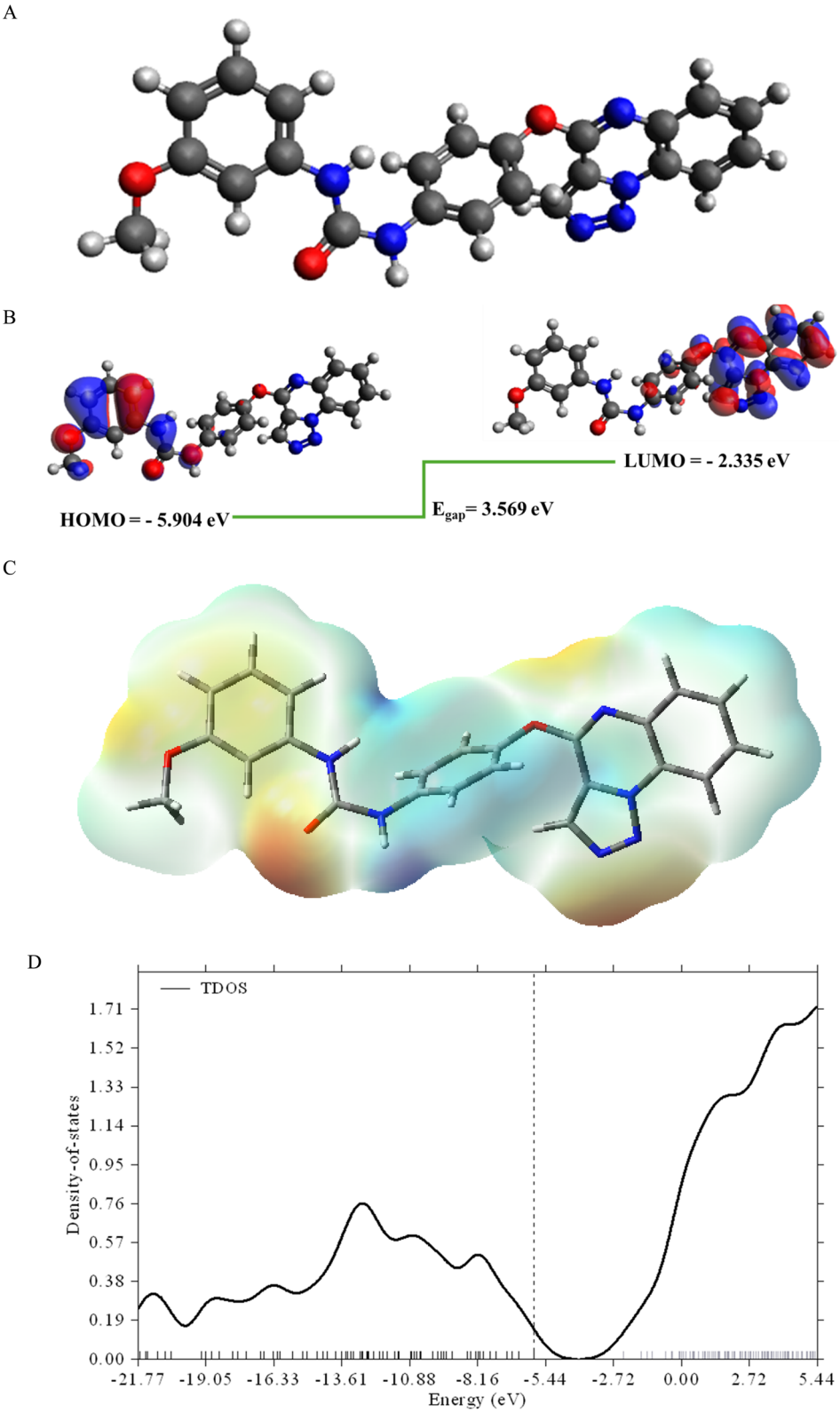


Fig. 13 The optimized structure (A), the HOMO/LUMO distribution function and energy gap (B), molecular electrostatic potential map (C) and total density of state (D) at B3LYP/6-31+G(d,p) level for **11d**.

inhibitory properties across these compounds are favorable for drug development. Compound **11a**, with its unique high BBB permeability, may be especially suitable for CNS-targeted therapies, while the low CNS exposure of the other compounds may be beneficial for peripheral applications. Improving solubility could further enhance their therapeutic profiles.

**2.3.9. *In silico* toxicity analysis.** The results in Table 10 provide insight into the toxicological and safety profiles of

Table 8 The global reactivity parameters for **11d** calculated through the DFT

| IP | EA | $\mu$ (eV) | $\chi$ (eV) | $\eta$ (eV) | $\sigma$ (eV) | $\omega$ (eV) | $D_m$ (debye) | TE (eV) | $\Delta N_{max}$ | $\Delta E$ (eV) |
|---|---|---|---|---|---|---|---|---|---|---|
| 5.904 | 2.335 | −4.120 | 4.120 | 1.784 | 0.560 | 15.142 | 4.279 | −39225.1 | 2.309 | −15.142 |

Table 9 Computational pharmacokinetic profile of compounds **11a–d**

| Comp. | BBB level | Solubility level | Absorption level | CYP2D6 prediction | PPB prediction |
|---|---|---|---|---|---|
| **11a** | High | Low | Good | Non inhibitor | More than 90% |
| **11b** | Very low | Very low | | | |
| **11c** | | | | | |
| **11d** | | Low | | | |
| Sorafenib | | Very low | | | |

compounds **11a**, **11b**, **11c**, and **11d** in comparison to sorafenib. Starting with carcinogenic potency and mutagenicity: the carcinogenic potency ($TD_{50}$) values indicate a general trend where compounds **11a** to **11d** exhibited variable carcinogenic potencies, with **11a** having the highest $TD_{50}$ value of 38.76 mg $kg^{-1}$, suggesting a lower carcinogenic risk relative to sorafenib ($TD_{50}$ = 14.24 mg $kg^{-1}$). All tested compounds were predicted to be non-mutagenic by the Ames test, contrasting with sorafenib, which is a single carcinogen. This may imply a potentially safer profile in terms of mutagenic risk for these compounds. Regarding the tolerated and lethal doses (MTD and $LD_{50}$): in examining the maximum tolerated dose (MTD) and $LD_{50}$ values for these compounds in rats, the data shows that compounds **11a** through **11d** have MTD values ranging from 0.065 to 0.147 mg $kg^{-1}$, which are relatively comparable but slightly higher than sorafenib (MTD = 0.0885 mg $kg^{-1}$). The $LD_{50}$ values of 11-series compounds are lower than sorafenib ($LD_{50}$ = 0.822 mg $kg^{-1}$), which suggests that they have lower acute toxicity, although further studies are needed to confirm these findings.

In the aspect of chronic exposure, the lowest observed adverse effect levels (LOAEL) indicate that compounds **11a** to **11d** present lower chronic toxicity levels compared to sorafenib. For instance, compound **11a**, with a LOAEL of 0.021 mg $kg^{-1}$, is less toxic than sorafenib (LOAEL = 0.0048 mg $kg^{-1}$), suggesting a potentially improved safety profile under long-term exposure. Skin and (SI) Eye Irritancy (EI): none of the 11-series compounds were found to be skin irritants, and all were categorized as mild ocular irritants. This aligns with sorafenib's profile, indicating a low likelihood of dermal toxicity.

In conclusion, the toxicological profile of the 11-series compounds shows potential advantages over sorafenib, particularly in terms of carcinogenic risk, chronic toxicity, and irritancy. However, additional studies, particularly *in vivo*, would be necessary to confirm the safety and efficacy of these compounds as therapeutic candidates.

The computational predictions suggest that **11d** exhibits notable pharmacokinetic advantages over sorafenib, particularly in terms of absorption, safety, and toxicity as follows. (i) Sorafenib is known for its poor aqueous solubility, which limits its bioavailability and necessitates high oral doses (400 mg twice daily) to achieve therapeutic plasma concentrations. The ADMET results indicate that compound **11d** has slightly better solubility than sorafenib, though it remains in the low-to-moderate range. Improved solubility enhances intestinal absorption, which could allow for lower dosing requirements, reducing systemic exposure to toxic metabolites. (ii) The ADMET predictions suggest that **11d** has good intestinal permeability, similar to sorafenib. (iii) Unlike compound **11a**, which has high BBB permeability, **11d** has low BBB penetration, similar to sorafenib. This is a desirable feature for anticancer drugs targeting VEGFR-2, as it minimizes potential neurological side effects, such as cognitive impairment, that are often associated with tyrosine kinase inhibitors (TKIs) with high CNS exposure. (iv) Both sorafenib and **11d** exhibit strong plasma protein binding (>90%), meaning that most of the drug remains bound to albumin and other plasma proteins. While high PPB can limit free drug availability, it also prolongs the half-life and may contribute to sustained drug action. The comparable PPB suggests that **11d** could have a half-life similar to, or potentially

Table 10 Computational toxicity profile of compounds **11a–d**

| Comp. | $TD_{50}$ (rat)[a] | Ames prediction | Mouse-female FDA | MTD | Rat oral $LD_{50}$[b] | Rat chronic LOAEL[b] | SI | EI |
|---|---|---|---|---|---|---|---|---|
| **11a** | 38.7633 | Non-mutagen | Non-carcinogen | 0.12016 | 0.203002 | 0.0213632 | Non-irritant | Mild |
| **11b** | 10.3763 | | | 0.147027 | 0.17387 | 0.017032 | | |
| **11c** | 10.3763 | | | 0.147027 | 0.275129 | 0.0158809 | | |
| **11d** | 3.12316 | | | 0.0655489 | 0.414131 | 0.0135571 | | |
| Sorafenib | 14.2442 | | Single-carcinogen | 0.088543 | 0.822583 | 0.00482816 | | |

[a] Unit: mg $kg^{-1}$ body weight per day. [b] Unit: g $kg^{-1}$ body weight.

longer than, sorafenib, though this needs to be validated with *in vivo* pharmacokinetic studies. (v) Sorafenib is classified as a single carcinogen, meaning it has some potential for long-term oncogenic effects. In contrast, compound **11d** is predicted to be non-mutagenic and non-carcinogenic, making it a potentially safer long-term therapy. (vi) The Maximum Tolerated Dose (MTD) of **11d** (0.065 mg $kg^{-1}$) is slightly higher than sorafenib (0.0885 mg $kg^{-1}$), suggesting that **11d** has a better safety margin. (vii) The Lowest Observed Adverse Effect Level (LOAEL) of **11d** (0.0136 mg $kg^{-1}$) is higher than sorafenib (0.0048 mg $kg^{-1}$), reinforcing its lower chronic toxicity potential. (viii) Unlike some kinase inhibitors that cause severe dermatological toxicity, **11d** is predicted to be non-irritant to the skin and a mild ocular irritant, similar to sorafenib. This suggests that **11d** may be better tolerated in long-term use.

# 3. Conclusion

In this study, we synthesized and evaluated a series of quinoxaline derivatives as potential VEGFR-2 inhibitors, focusing on their anti-cancer properties against breast cancer cells. Compound **11d** demonstrated notable selectivity and efficacy, exhibiting potent cytotoxic effects on MDA-MB-231 and MCF-7 cancer cell lines while showing reduced toxicity in normal cell lines. Mechanistic studies revealed that **11d** effectively inhibited VEGFR-2, induced apoptosis by upregulating pro-apoptotic genes, and significantly impaired cancer cell migration and cell cycle progression. Furthermore, *in silico* analyses, including molecular docking, molecular dynamics simulations, ProLIF, PCA, FEL and DFT calculations, indicated strong and stable binding of **11d** to VEGFR-2, along with a favorable ADMET profile, positioning it as a safer alternative to sorafenib. Collectively, our findings highlight **11d** as a promising candidate for targeted anti-angiogenic therapy. Further preclinical studies are warranted to validate these effects *in vivo* and assess the therapeutic potential of **11d** in combination with current cancer treatments. For future directions, we hope to carry out the following tasks. *In vivo* efficacy studies to evaluate the tumor suppression ability of **11d**. Further studies should assess half-life, metabolism, and biodistribution *in vivo*. Further modifications could improve solubility and oral bioavailability. Evaluating **11d** in combination with standard chemotherapies could determine synergistic effects.

# 4. Experimental

## 4.1. Chemistry

**4.1.1. General procedure for synthesis of the key intermediates 10a–d.** *P*-Aminophenol **8** (5 mmol) was added to a stirred solution of isocyanate derivatives **9a–d** (13 mmol) in acetonitrile (100 mL). At room temperature, the reaction mixture was agitated, and TLC was used to track its development (DCM : methanol = 9 : 1). Compounds **10a–d** were obtained by filtering, washing with acetonitrile, and drying the precipitate.[61]

**4.1.2. General procedure for synthesis of the final target compounds 11a–d.** 4-Chloro-[1,2,4]triazolo[4,3-*a*]quinoxaline **7** (2 mmol, 0.41 g) was added to a stirred solution of compounds **10a–d** (2 mmol) and TEA (2 mmol) in tetrahydrofuran (20 mL) at reflux temperature. The reaction was then continued at room temperature and monitored using TLC. Following completion of the reaction, the precipitates were filtered and recrystallized from ethanol to provide the desired target compounds **11a–d.**

*4.1.2.1. 1-(4-([1,2,4]Triazolo[4,3-a]quinoxalin-4-yloxy) phenyl)-3-phenylurea **11a**.*

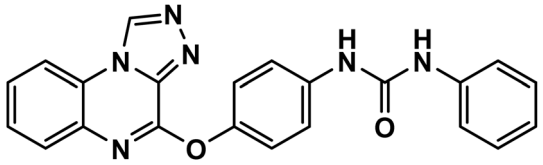

White powder (yield, 75%); mp = 213–215 °C. FT-IR ($\nu_{max}$, $cm^{-1}$): 3421, 3119 (NH), 3060 (C–H aromatic), 2925, 2830 (C–H aliphatic), 1682 (C=O); $^1$H NMR (400 MHz, DMSO-$d_6$) $\delta$ 10.17 (s, 1H, CH triazolo), 8.88 (s, 1H, NH), 8.85 (s, 1H, NH), 8.37 (d, $J$ = 8.1 Hz, 1H, Ar–H), 7.76–7.48 (m, 8H, Ar–H), 7.35 (dd, $J$ = 8.6, 6.1 Hz, 4H, Ar–H); $^{13}$C NMR (101 MHz, DMSO-$d_6$) $\delta$ 153.03, 151.72, 146.74, 139.19, 138.77, 138.73, 137.75, 134.34, 129.11, 128.30, 128.21, 127.78, 125.85, 124.54, 122.70, 120.23, 120.04, 116.92; mass ($m/z$): 396 ($M^+$, 57.84%), 381 (100%, base peak); anal. calcd for $C_{22}H_{16}N_6O_2$ (396.41): C, 66.66; H, 4.07; N, 21.20. Found: C, 66.92; H, 4.21; N, 21.43%.

*4.1.2.2. 1-(4-([1,2,4]Triazolo[4,3-a]quinoxalin-4-yloxy) phenyl)-3-(3-chlorophenyl)urea **11b**.*

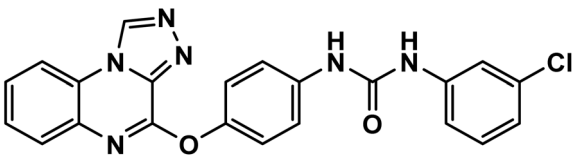

White powder (yield, 77%); mp = 207–209 °C. FT-IR ($\nu_{max}$, $cm^{-1}$): 3331, 3103 (NH), 3067, 3014 (C–H aromatic), 1682 (C=O); $^1$H NMR (500 MHz, DMSO-$d_6$) $\delta$ 10.13 (s, 1H, CH triazolo), 8.91 (s, 1H, NH), 8.86 (s, 1H, NH), 8.33 (dd, $J$ = 8.1, 1.4 Hz, 1H, Ar–H), 7.69 (q, $J$ = 1.5 Hz, 1H, Ar–H), 7.64–7.58 (m, 2H, Ar–H), 7.56–7.50 (m, 3H, Ar–H), 7.32 (d, $J$ = 2.2 Hz, 1H, Ar–H), 7.31–7.29 (m, 1H, Ar–H), 7.28–7.24 (m, 2H, Ar–H), 6.98 (dt, $J$ = 6.7, 2.3 Hz, 1H, Ar–H); $^{13}$C NMR (126 MHz, DMSO-$d_6$) $\delta$ 153.06, 151.76, 147.00, 141.83, 138.81, 137.68, 134.44, 133.77, 130.91, 128.37, 128.31, 127.87, 124.64, 122.71, 122.04, 120.25, 118.23, 117.28, 116.99; mass ($m/z$): 430 ($M^+$, 22.40%), 402 (100%, base peak); anal. calcd for $C_{22}H_{15}ClN_6O_2$ (430.85): C, 61.33; H, 3.51; N, 19.51. Found: C, 61.60; H, 3.79; N, 19.68%.

*4.1.2.3. 1-(4-([1,2,4]Triazolo[4,3-a]quinoxalin-4-yloxy) phenyl)-3-(4-chlorophenyl)urea **11c**.*

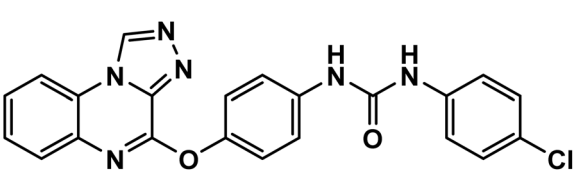

White powder (yield, 78%); mp = 200–202 °C. FT-IR ($\nu_{max}$, $cm^{-1}$): 3320 (NH), 3056 (C–H aromatic), 2920 (C–H aliphatic),

1654 (C=O); $^1$H NMR (500 MHz, DMSO-$d_6$) $\delta$ 10.13 (s, 1H, CH triazolo), 8.84 (s, 1H, NH), 8.81 (s, 1H, NH), 8.33 (dd, $J$ = 8.2, 1.4 Hz, 1H, Ar–H), 7.65–7.58 (m, 2H, Ar–H), 7.56–7.50 (m, 3H, Ar–H), 7.49–7.45 (m, 2H, Ar–H), 7.32–7.28 (m, 4H, Ar–H); $^{13}$C NMR (126 MHz, DMSO-$d_6$) $\delta$ 153.14, 151.73, 147.05, 139.27, 138.82, 138.76, 137.79, 134.47, 129.12, 128.35, 128.32, 127.86, 126.08, 124.66, 122.62, 120.47, 120.20, 116.97; mass ($m/z$): 430 ($M^+$, 34.27%), 48 (100%, base peak); anal. calcd for $C_{22}H_{15}ClN_6O_2$ (430.85): C, 61.33; H, 3.51; N, 19.51. Found: C, 61.58; H, 3.75; N, 19.59%.

*4.1.2.4. 1-(4-([1,2,4]Triazolo[4,3-a]quinoxalin-4-yloxy) phenyl)-3-(3-methoxyphenyl)urea* ***11d****.*

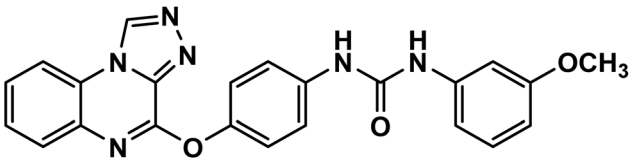

White powder (yield, 80%); mp = 208–210 °C. FT-IR ($\nu_{max}$, cm$^{-1}$): 3327, 3103 (NH), 3067, 3014 (C–H aromatic), 2915 (C–H aliphatic), 1679 (C=O); $^1$H NMR (400 MHz, DMSO-$d_6$) $\delta$ 10.16 (s, 1H, CH triazolo), 8.79 (s, 1H, NH), 8.74 (s, 1H, NH), 8.36 (d, $J$ = 8.1 Hz, 1H, Ar–H), 7.68–7.54 (m, 6H, Ar–H), 7.34 (d, $J$ = 8.5 Hz, 2H, Ar–H), 7.25–7.13 (m, 2H, Ar–H), 6.96 (d, $J$ = 8.0 Hz, 1H, Ar–H), 6.61–6.52 (m, 1H, Ar–H), 3.74 (s, 3H, $OCH_3$); $^{13}$C NMR (101 MHz, DMSO-$d_6$) $\delta$ 160.17, 153.06, 151.72, 146.66, 141.36, 138.76, 138.73, 137.84, 134.33, 130.05, 128.33, 128.21, 127.80, 124.52, 122.68, 119.98, 116.91, 111.04, 107.75, 104.49, 55.41; mass ($m/z$): 426 ($M^+$, 33.73%), 350 (100%, base peak); anal. calcd for $C_{23}H_{18}N_6O_3$ (426.44): C, 64.78; H, 4.25; N, 19.71. Found: C, 64.67; H, 4.48; N, 19.95%.

### 4.2. *In vitro* studies

**4.2.1. Cytotoxicity.** The cytotoxicity and selectivity of compounds **11a–d** and the reference drug were evaluated against cell lines (MDA-231, MCF-7, WI-38, and WISH) using the MTT assay[62–64] (ESI†).

**4.2.2. Enzyme inhibition.** The inhibitory activities of compound **11d** and reference drug against VEGFR-2 were tested using enzyme assay kits at concentrations ranging from 0.3 to 1000 nM[65,66] (ESI†).

**4.2.3. RT-qPCR studies.** The expression levels of apoptosis-related genes (BAX, Bcl-2, caspase-8, and caspase-9) in MDA-MB-231 cells treated with **11d** (16.13 μM) were measured using qRT-PCR, following established protocols[67] (ESI†).

**4.2.4. Flow cytometry.** The effects of **11d** on apoptosis and cell cycle progression in MDA-MB-231 cells were analyzed using flow cytometry[68,69] (ESI†).

### 4.3. Computational studies

**4.3.1. Molecular docking.** Molecular docking simulations for compounds **11a–d** and reference drug against VEGFR-2 were performed as described in ESI.†

**4.3.2. Molecular dynamics (MD) simulations.** MD simulations were carried out for the VEGFER-2-**11d** complexe using the CHARMM-GUI web server and GROMACS 2021 software.[70,71] The binding free energies of **11d** were calculated using the gmx_MMPBSA tool with the MM-GBSA method.[72,73] Principal component analysis (PCA) was used to analyze the dynamic motions of alpha carbons in specific amino acid sequences.[74] The free energy landscape (FEL) of the protein was studied in terms of two defined states, with their probabilities connected through an exponential relationship.[75] (ESI†).

**4.3.3. ADMET and toxicity.** The pharmacokinetic and toxicity profiles of compounds **11a–d** were predicted using Discovery Studio 4.0 software[76] (ESI†).

**4.3.4. Density functional theory (DFT).** The structural optimization and reactivity analysis of **11d** were performed using the Gaussian 09 (D.01) software with the DFT method, employing the B3LYP functional and the 6-31+G(d,p) basis set.[77] Detailed methods are available in the ESI.†

## Data availability

Data are available in the manuscript and the ESI.†

## Conflicts of interest

No conflict of interest to be declared.

## Acknowledgements

This research was funded by Princess Nourah bint Abdulrahman University Researchers Supporting Project Number (PNURSP2025R116), Princess Nourah bint Abdulrahman University, Riyadh, Saudi Arabia. The authors would like to thank Research Center at AlMaarefa University for funding this work.

## References

1 S. M. Schwartz, *Clin. Chem.*, 2024, **70**, 140–149.
2 D. Trapani, O. Ginsburg, T. Fadelu, N. U. Lin, M. Hassett, A. M. Ilbawi, B. O. Anderson and G. Curigliano, *Cancer Treat Rev.*, 2022, **104**, 102339.
3 L. Wilkinson and T. Gathani, *Br. J. Radiol.*, 2022, **95**, 20211033.
4 A. A. Shah, M. A. Kamal and S. Akhtar, *Curr. Drug Metab.*, 2021, **22**, 50–59.
5 M. S. Taghour, H. Elkady, W. M. Eldehna, N. El-Deeb, A. M. Kenawy, A. E. Abd El-Wahab, E. B. Elkaeed, B. A. Alsfouk, A. M. Metwaly and I. H. Eissa, *J. Biomol. Struct. Dyn.*, 2023, **41**, 11535–11550.
6 X. J. Liu, H. C. Zhao, S. J. Hou, H. J. Zhang, L. Cheng, S. Yuan, L. R. Zhang, J. Song, S. Y. Zhang and S. W. Chen, *Bioorg. Chem.*, 2023, **133**, 106425.
7 E. B. Elkaeed, R. G. Yousef, H. Elkady, A. B. Mehany, B. A. Alsfouk, D. Z. Husein, I. M. Ibrahim, A. M. Metwaly and I. H. Eissa, *J. Biomol. Struct. Dyn.*, 2023, **41**, 7986–8001.
8 M. Montana, F. Mathias, T. Terme and P. Vanelle, *Eur. J. Med. Chem.*, 2019, **163**, 136–147.

9 V. Montero, M. Montana, M. Carré and P. Vanelle, *Eur. J. Med. Chem.*, 2024, **271**, 116360.
10 M. Zayed, *Chemistry*, 2023, **5**, 2566–2587.
11 M. S. Nafie, S. H. Kahwash, M. M. Youssef and K. M. Dawood, *Arch. Pharm.*, 2024, **357**, e2400225.
12 M. A. Dahab, H. A. Mahdy, H. Elkady, M. S. Taghour, A. Elwan, M. A. Elkady, E. G. E. Elsakka, E. B. Elkaeed, A. A. Alsfouk, I. M. Ibrahim, A. M. Metwaly and I. H. Eissa, *J. Biomol. Struct. Dynam.*, 2024, **42**, 4214–4233.
13 A. M. Metwaly, H. Abd-El-Azim, M. Zewail, A. A. Alsfouk, E. B. Elkaeed and I. H. Eissa, *J. Comput. Biophys. Chem.*, 2024, 1–17.
14 I. H. Eissa, R. G. Yousef, H. Elkady, A. A. Alsfouk, D. Z. Husein, I. M. Ibrahim, N. El-Deeb, A. M. Kenawy, W. M. Eldehna, E. B. Elkaeed and A. M. Metwaly, *Mol. Divers.*, 2024, **28**, 1153–1173.
15 I. H. Eissa, R. G. Yousef, E. B. Elkaeed, A. A. Alsfouk, D. Z. Husein, I. M. Ibrahim, A. Ismail, H. Elkady and A. M. Metwaly, *ACS Omega*, 2024, **9**, 15861–15881.
16 E. A. Sobh, M. A. Dahab, E. B. Elkaeed, A. A. Alsfouk, I. M. Ibrahim, A. M. Metwaly and I. H. Eissa, *J. Biomol. Struct. Dynam.*, 2024, **42**, 2369–2391.
17 I. H. Eissa, R. G. Yousef, E. B. Elkaeed, A. A. Alsfouk, D. Z. Husein, I. M. Ibrahim, H. A. El-Mahdy, H. Elkady and A. M. Metwaly, *Evol. Bioinf. Online*, 2023, **19**, 11769343231217916.
18 K. El-Adl, H. M. Sakr, R. G. Yousef, A. B. M. Mehany, A. M. Metwaly, M. A. Elhendawy, M. M. Radwan, M. A. ElSohly, H. S. Abulkhair and I. H. Eissa, *Bioorg. Chem.*, 2021, **114**, 105105.
19 R. G. Yousef, H. M. Sakr, I. H. Eissa, A. B. Mehany, A. M. Metwaly, M. A. Elhendawy, M. M. Radwan, M. A. ElSohly, H. S. Abulkhair and K. El-Adl, *New J. Chem.*, 2021, **45**, 16949–16964.
20 I. H. Eissa, A. M. Metwaly, A. Belal, A. B. M. Mehany, R. R. Ayyad, K. El-Adl, H. A. Mahdy, M. S. Taghour, K. M. A. El-Gamal, M. E. El-Sawah, S. A. Elmetwally, M. A. Elhendawy, M. M. Radwan and M. A. ElSohly, *Arch. Pharm.*, 2019, **352**, e1900123.
21 M. K. Ibrahim, M. S. Taghour, A. M. Metwaly, A. Belal, A. B. M. Mehany, M. A. Elhendawy, M. M. Radwan, A. M. Yassin, N. M. El-Deeb, E. E. Hafez, M. A. ElSohly and I. H. Eissa, *Eur. J. Med. Chem.*, 2018, **155**, 117–134.
22 M. K. Ibrahim, I. H. Eissa, A. E. Abdallah, A. M. Metwaly, M. M. Radwan and M. A. ElSohly, *Bioorg. Med. Chem.*, 2017, **25**, 1496–1513.
23 Y. Liu, Y. Li, Y. Wang, C. Lin, D. Zhang, J. Chen, L. Ouyang, F. Wu, J. Zhang and L. Chen, *J. Hematol. Oncol.*, 2022, **15**, 89.
24 S. Fogli, C. Porta, M. Del Re, S. Crucitta, G. Gianfilippo, R. Danesi, B. I. Rini and M. Schmidinger, *Cancer Treat Rev.*, 2020, **84**, 101966.
25 E. S. Duke, A. K. Barone, S. Chatterjee, P. S. Mishra-Kalyani, Y.-L. Shen, E. Isikwei, H. Zhao, Y. Bi, J. Liu and N. A. Rahman, *Clin. Cancer Res.*, 2022, **28**, 4173–4177.
26 N. Agarwal, A. Azad, J. Carles, S. Chowdhury, B. McGregor, A. S. Merseburger, S. Oudard, F. Saad, A. Soares and F. Benzaghou, *Future Oncol.*, 2022, **18**, 1185–1198.
27 S. M. Ferrari, M. Centanni, C. Virili, M. Miccoli, P. Ferrari, I. Ruffilli, F. Ragusa, A. Antonelli and P. Fallahi, *Curr. Med. Chem.*, 2019, **26**, 963–972.
28 B. Chaudhari, H. Patel, S. Thakar, I. Ahmad and D. Bansode, *In Silico Pharmacol.*, 2022, **10**, 10.
29 D. Pink, D. Andreou, S. Bauer, T. Brodowicz, B. Kasper, P. Reichardt, S. Richter, L. H. Lindner, J. Szkandera and V. Grünwald, *Cancers*, 2021, **13**, 1223.
30 Y. Pang, A. Eresen, Z. Zhang, Q. Hou, Y. Wang, V. Yaghmai and Z. Zhang, *Am. J. Cancer Res.*, 2022, **12**, 2770.
31 A.-L. Cheng, S. Qin, M. Ikeda, P. R. Galle, M. Ducreux, T.-Y. Kim, H. Y. Lim, M. Kudo, V. Breder and P. Merle, *J. Hepatol.*, 2022, **76**, 862–873.
32 B. Liang, M. Tang, C. Huang, Y. Yang, Y. He, S. Liao and W. Shen, *J. Gastrointest. Cancer*, 2025, **56**, 36.
33 J. Guo, J. Zhao, Q. Xu and D. Huang, *Curr. Cancer Drug Targets*, 2022, **22**, 865–878.
34 L. J. Scott, *Drugs*, 2015, **75**, 553–560.
35 P. Norman, *Expert Opin. Orphan Drugs*, 2015, **3**, 445–455.
36 R. Elisei, M. J. Schlumberger, S. P. Müller, P. Schöffski, M. S. Brose, M. H. Shah, L. Licitra, B. Jarzab, V. Medvedev and M. C. Kreissl, *J. Clin. Oncol.*, 2013, **31**, 3639.
37 S. Wilhelm, C. Carter, M. Lynch, T. Lowinger, J. Dumas, R. A. Smith, B. Schwartz, R. Simantov and S. Kelley, *Nat. Rev. Drug Discov.*, 2006, **5**, 835–844.
38 S. M. Wilhelm, J. Dumas, L. Adnane, M. Lynch, C. A. Carter, G. Schütz, K. H. Thierauch and D. Zopf, *Int. J. Cancer*, 2011, **129**, 245–255.
39 H. Y. Woo and J. Heo, *Expet Opin. Pharmacother.*, 2012, **13**, 1059–1067.
40 S. DiGiulio, *Oncology Times*, 2013.
41 Y. Li, Z. H. Gao and X. J. Qu, *Basic Clin. Pharmacol. Toxicol.*, 2015, **116**, 216–221.
42 S. K. Krishnamoorthy, V. Relias, S. Sebastian, V. Jayaraman and M. W. Saif, *Ther. Adv. Gastroenterol.*, 2015, **8**, 285–297.
43 C. Grüllich, in *Small Molecules in Oncology*, Springer, 2014, pp. 207–214.
44 C. Zhu, X. Ma, Y. Hu, L. Guo, B. Chen, K. Shen and Y. Xiao, *Oncotarget*, 2016, **7**, 44545.
45 F.-W. Peng, D.-K. Liu, Q.-W. Zhang, Y.-G. Xu and L. Shi, *Expert Opin. Ther. Pat.*, 2017, **27**, 987–1004.
46 M. M. Alanazi, H. Elkady, N. A. Alsaif, A. J. Obaidullah, W. A. Alanazi, A. M. Al-Hossaini, M. A. Alharbi, I. H. Eissa and M. A. Dahab, *J. Mol. Struct.*, 2021, 132220.
47 K. Lee, K.-W. Jeong, Y. Lee, J. Y. Song, M. S. Kim, G. S. Lee and Y. Kim, *Eur. J. Med. Chem.*, 2010, **45**, 5420–5427.
48 V. A. Machado, D. Peixoto, R. Costa, H. J. Froufe, R. C. Calhelha, R. M. Abreu, I. C. Ferreira, R. Soares and M.-J. R. Queiroz, *Bioorg. Med. Chem.*, 2015, **23**, 6497–6509.
49 Z. Wang, N. Wang, S. Han, D. Wang, S. Mo, L. Yu, H. Huang, K. Tsui, J. Shen and J. Chen, *PLoS One*, 2013, **8**, e68566.
50 J. Dietrich, C. Hulme and L. H. Hurley, *Bioorg. Med. Chem.*, 2010, **18**, 5738–5748.
51 Q.-Q. Xie, H.-Z. Xie, J.-X. Ren, L.-L. Li and S.-Y. Yang, *J. Mol. Graph. Model.*, 2009, **27**, 751–758.
52 R. N. Eskander and K. S. Tewari, *Gynecol. Oncol.*, 2014, **132**, 496–505.

53 M. Ibrahim, M. Taghour, A. M. Metwaly, A. Belal, A. Mehany, M. Elhendawy, M. Radwan, A. Yassin, N. El-Deeb and E. Hafez, *Eur. J. Med. Chem.*, 2018, **155**, 117–134.
54 I. H. Eissa, A. M. Metwaly, A. Belal, A. B. Mehany, R. R. Ayyad, K. El-Adl, H. A. Mahdy, M. S. Taghour, K. M. El-Gamal and M. E. El-Sawah, *Arch. Pharm.*, 2019, **352**, 1900123.
55 E. M. Abbass, A. K. Khalil, M. M. Mohamed, I. H. Eissa and A. M. El-Naggar, *Bioorg. Chem.*, 2020, **104**, 104255.
56 N. A. Alsaif, M. A. Dahab, M. M. Alanazi, A. J. Obaidullah, A. A. Al-Mehizia, M. M. Alanazi, S. Aldawas, H. A. Mahdy and H. Elkady, *Bioorg. Chem.*, 2021, **110**, 104807.
57 N. A. Alsaif, M. S. Taghour, M. M. Alanazi, A. J. Obaidullah, A. A. Al-Mehizia, M. M. Alanazi, S. Aldawas, A. Elwan and H. Elkady, *J. Enzym. Inhib. Med. Chem.*, 2021, **36**, 1093–1114.
58 F. Azimian, M. Hamzeh-Mivehroud, J. S. Mojarrad, S. Hemmati and S. Dastmalchi, *Eur. J. Med. Chem.*, 2020, **201**, 112461.
59 D. Z. Husein, R. Hassanien and M. Khamis, *RSC Adv.*, 2021, **11**, 27027–27041.
60 R. G. Parr, L. v. Szentpály and S. Liu, *J. Am. Chem. Soc.*, 1999, **121**, 1922–1924.
61 R. G. Gieling, M. Babur, L. Mamnani, N. Burrows, B. A. Telfer, F. Carta, J.-Y. Winum, A. Scozzafava, C. T. Supuran and K. J. Williams, *J. Med. Chem.*, 2012, **55**, 5591–5600.
62 A. R. Kotb, D. A. Bakhotmah, A. E. Abdallah, H. Elkady, M. S. Taghour, I. H. Eissa and M. A. El-Zahabi, *RSC Adv.*, 2022, **12**, 33525–33539.
63 A. R. Kotb, A. E. Abdallah, H. Elkady, I. H. Eissa, M. S. Taghour, D. A. Bakhotmah, T. M. Abdelghany and M. A. El-Zahabi, *RSC Adv.*, 2023, **13**, 10488–10502.
64 A. Saha, S. Mohapatra, P. Kurkute, B. Jana, J. Sarkar, P. Mondal and S. Ghosh, *RSC Adv.*, 2015, **5**, 92596–92601.
65 H. A. Mahdy, H. Elkady, M. S. Taghour, A. Elwan, M. A. Dahab, M. A. Elkady, E. G. Elsakka, E. B. Elkaeed, B. A. Alsfouk and I. M. Ibrahim, *Future Med. Chem.*, 2023, **15**, 1233–1250.
66 A. E. Abdallah, R. R. Mabrouk, M. R. Elnagar, A. M. Farrag, M. H. Kalaba, M. H. Sharaf, E. M. El-Fakharany, D. A. Bakhotmah, E. B. Elkaeed and M. M. S. Al Ward, *Drug Des., Dev. Ther.*, 2023, 587–606.
67 K. J. Livak and T. D. Schmittgen, *Methods*, 2001, **25**, 402–408.
68 Z. Darzynkiewicz, E. Bedner and P. Smolewski, Flow cytometry in analysis of cell cycle and apoptosis, *Seminars in hematology*, Elsevier, 2001, pp. 179–193.
69 D. Bhunia, A. Saha, A. Adak, G. Das and S. Ghosh, *RSC Adv.*, 2016, **6**, 113487–113491.
70 B. R. Brooks, C. L. Brooks III, A. D. Mackerell Jr, L. Nilsson, R. J. Petrella, B. Roux, Y. Won, G. Archontis, C. Bartels and S. Boresch, *J. Comput. Chem.*, 2009, **30**, 1545–1614.
71 S. Jo, X. Cheng, S. M. Islam, L. Huang, H. Rui, A. Zhu, H. S. Lee, Y. Qi, W. Han and K. Vanommeslaeghe, *Adv. Protein Chem. Struct. Biol.*, 2014, **96**, 235–265.
72 T. Tuccinardi, *Expet Opin. Drug Discov.*, 2021, **16**, 1233–1237.
73 M. S. Valdés-Tresanco, M. E. Valdés-Tresanco, P. A. Valiente and E. Moreno, *J. Chem. Theor. Comput.*, 2021, **17**, 6281–6291.
74 A. Amadei, A. B. Linssen and H. J. Berendsen, *Proteins: Struct., Funct., Bioinf.*, 1993, **17**, 412–425.
75 E. Papaleo, P. Mereghetti, P. Fantucci, R. Grandori and L. De Gioia, *J. Mol. Graph. Model.*, 2009, **27**, 889–899.
76 A. M. Metwaly, E. B. Elkaeed, B. A. Alsfouk, A. M. Saleh, A. E. Mostafa and I. H. Eissa, *Plants*, 2022, **11**, 1886.
77 D. S. Biovia, *Discovery studio modeling environment*, Release San Diego, CA, 2017.